LABORATORY WIND TUNNEL EXPERIMENT ON DUST GENERATION DURING THE SALTATION OF AGGREGATES FORMED FROM OWENS LAKE PLAYA SEDIMENTS

A Thesis Submitted to the Committee on Graduate Studies in Partial Fulfillment of the Requirements for the Degree of Master of Science in the Faculty of Arts and Science

TRENT UNIVERSITY

Peterborough, Ontario, Canada

Environmental and Life Sciences M.Sc. Graduate Program

May 2023

ABSTRACT

LABORATORY WIND TUNNEL EXPERIMENT OF DUST GENERATION DURING THE SALTATION OF AGGREGATES FORMED FROM OWENS LAKE PLAYA SEDIMENTS

Gianna Isabella Saarenvirta

This study reports on as series of laboratory wind tunnel experiments aimed at furthering our understanding of aggregate breakdown and dust release during aeolian transport, and thereby, has implications for air quality and the management of dust emission through water application. Particles aggregates 500 μm in diameter were formed and isolated by the wetting, drying, and screening of playa sediments collected from Owens Lake. They were then released into a boundary-layer flow within the Trent Environmental Wind Tunnel (TEWT), whereupon they either slid, rolled and/or saltated downwind. The concentration of PM_{10} and the particle size of the aggregates were monitored throughout each test along the central axis of the tunnel. The results confirm that aggregate breakdown did occur, resulting in the production and emission of dust. The relative efficiency of aggregate abrasion in the production of silt sized particles during aeolian transport was calculated using normalized indices, providing a starting point for the modelling of similar systems in a natural setting. The results indicate that for every metre of transport, the abrasion of a 500 μm aggregate formed from playa sediment may release a volume of dust roughly equivalent to that of a single silt particle that is 60 μm diameter. Conversely, aggregate formation is found to produce 1-4% of dust as compared to an equivalent volume of disaggregated silt when exposed to a given airflow above the threshold for saltation.

KEYWORDS

Wind tunnel, PM_{10}, Owens Lake, soil aggregation, aggregate breakdown, dust emission, saltation, aeolian abrasion, playas

ACKNOWLEDGMENTS

Throughout the writing of this thesis, I have received a great deal of support and assistance.

I would first like to thank my supervisor, Dr. Cheryl McKenna-Neuman, whose expertise was invaluable in creating the research questions and methodology. Your insightful feedback pushed me to sharpen my thinking and brought my work and writing skills to a higher level.

I would like to acknowledge the wind tunnel technician, Dr. Patrick O'Brien, for his wonderful help and collaboration in helping my methodology come to life, as well as creating the code crucial for my analysis. Also, Christopher Schweighofer, a fellow graduate student, who was instrumental in the collection of my data. You both provided me with the tools I needed to successfully complete my thesis.

Dr. Joanna Bullard of the materials science lab in Loughborough University, and Dr. Ian Power both contributed to this work as they aided in the collection of data for the particle chemistry and SEM analysis.

In addition, I would like to acknowledge NSERC who supported me with an undergraduate award that supplied me with the resources to train in preparation of my thesis. I could not have completed this thesis without the opportunities I was given to further my research and knowledge.

Lastly, I would like to thank CFI, who administered funding for equipment that provided the DustTrak's and LDA. This research would not have been possible without the technology provided by you through that grant.

TABLE OF CONTENTS

LIST OF TABLES

LIST OF FIGURES

LIST OF SYMBOLS AND ACRONYMS

LDA: Laser Doppler Anemometer

TEWT: Trent University Environmental Wind Tunnel

PM_{10}: particulate matter < 10 µm in diameter

u_*: shear velocity (ms^{-1})

k: Von Karmen constant (0.4)

u_z: streamwise velocity at height z (ms^{-1})

z: elevation (m)

z_o: aerodynamic roughness length (m)

i: elevation slice number

m_i: mass transport rate (mgs^{-1})

C_i: PM_{10} concentration at elevation i (mgm^{-3})

Δz: change in elevation (m)

u_i: particle velocity at elevation i (ms^{-1})

w: width of tunnel (m)

M: vertically integrated mass transport rate (mgs^{-1})

j: control volume reference number

A_{sj}: basal area of control volume j (m^2)

L: length of control volume (m)

Q_j: mass flux rate of control volume j ($mgm^{-2}s^{-1}$)

$M_j$out: vertically integrated mass transport rate output (mgs^{-1})

$M_j$in: vertically integrated mass transport rate input (mgs^{-1})

V_t: settling velocity (ms^{-1})

g: gravitational acceleration (9.8 ms^{-2})

d: particle diameter (m)

ρ_p: particle density (kgm^{-3})

ρ_m: density of medium (kgm^{-3})

µ: viscosity ($kgm^{-1}s^{-1}$)

u_p: horizontal particle velocity (ms^{-1})

v_p: vertical particle velocity (ms^{-1})

Chapter One: Introduction

1.1 Wind Erosion and PM_{10}

Wind erosion, resulting in dust emissions and a loss of topsoil in dryland environments, is a threat to environmental and human health (Duniway et al., 2019). Dryland environments are defined as areas with an aridity index, calculated as the ratio between mean annual precipitation (P) and mean annual potential evapotranspiration (PET), of ≤0.5 in the United States western regions (Schlaepfer et al., 2017). A process that is common in these dryland regions is the emission of particulate matter that is less than 10 microns in diameter (PM_{10}) into the atmosphere (Avecilla, 2016). Emission of PM_{10} depends on the texture and the aggregate (a group of particles that are bound together stronger than the surrounding particles) state, but also is governed by the mechanisms that produce and suspend dust (Avecilla, 2016). Managing wind erosion and dust emission in US drylands is challenging due to complex forces such as land use, climate, economics, soils, etc. (Duniway et al., 2019). Although wind erosion and dust emission are related, it is important to differentiate between the two as they have different environmental and human impacts (Duniway et al., 2019). Wind erosion describes the net loss of soil material, such as organic matter loss, that can represent a loss of nutrients as well as water retention capacity from soil (Duniway et al., 2019). Dust refers to airborne particulate matter that is entrained into the atmosphere and represents a risk to human health as the small particles can deeply penetrate the lung, resulting in several cardiovascular diseases. St. Amand et al. (1986) and Manisalidis et al. (2020) describe the environmental effects and respiratory illnesses that are associated with inhaling dust, such as asthma and chronic obstructive pulmonary disease (COPD).

1.2 Dust Emissions at Owens Lake Playa

Dry lake beds, or playas, are recognized as major sources of dust in dryland areas across the globe where evaporation exceeds water recharge. One such hydrological and geological feature resulting from the accumulation of groundwater discharge and surface water runoff is Owens Lake, California. Owens Lake was a saline lake located in eastern-central California (National, 2020). In the early 1900's, water was diverted from the Owens River, which is the main source of water for the lake, into the Los Angeles Aqueduct (National, 2020). The climate in the Owens Valley is semi-arid to arid with low precipitation, abundant sunshine, warm temperatures, moderate to low humidity and high PET (Hollett et al., 1991). This ultimately resulted in the lake drying out, leaving a hypersaline brine a fraction of the size of the original lake, mainly containing sodium sulphate and sodium chloride, easily erodible dry saline silty soils and fragile salts crusts (National, 2020).

Blowing dust became a large issue at Owens Lake as the dry bed contained several areas with sandy sediments, which can abrade dust from weak crusts and soil aggregates during wind events. This compounded the erodibility of the lakebed, creating large amounts of airborne dust (Gill and Cahill, 1992; National, 2020). This resulted in the highest concentrations of PM_{10} in the country, seeing a 24-hour maximum of 20,000 $\mu g/m^3$ in 2001 (National, 2020). This extreme concentration of mineral aerosol can be transported hundreds of kilometers downwind to critical ecological areas and several cities (National, 2020). With increased environmental awareness, there has been increasing interest in documenting the severity and hazards associated with these dust storms, along with researching mitigation methods. Studies of Owens Lake and its dust storms began in the early 1980's and have been funded by the State of California, the China Lake Naval Weapons Center, NOAA, EPA, and the USGS, collectively spending $2.1 billion as of May 2019 (National, 2020). These studies include

long-term monitoring of ambient aerosols (Barone et al., 1981; Cahill et al., 1994), measurements of dust storms at sites around the lake bed (Reid et al., 1994; Cahill et al., 1996), hourly monitoring of weather, sand movement, and surface conditions on the south end of the lake bed, satellite and airborne observations of dust storms (St. Amand et al., 1986), detailed sampling and analysis of lake-bed crusts and subsurface deposits (St. Amand et al., 1986; Cahill et al., 1996), and measurement of dust composition and deposition rates on and downwind of the lake bed (Reheis, 1997).

Current mitigation methods are undertaken by the Los Angeles Department of Water and Power, who owns Owens Lake. They are mainly shallow-flooding sections of the dried lakebed from deep aquifers, characterized as anoxic due to the high pH (9.3-10) and high electrical conductivity (3-54 $ds \bullet m^{-1}$) (Dahlgren et al., 1997). Adding salt rich water to an area with a high PET (15-40 inches/yr.) poses problems as the process of evapotranspiration reduces the volume of water and increases the concentration of salts in the water (Hollett et al., 1991; Freedman et al., 2014). This can leave large deposits of salt after the water evaporates off, resulting in poor health and fragile soils devoid of vegetation. Other mitigation methods include armouring of surface using gravel, sand fences, tillage, adding surface roughness, brine, as well as planting salt-tolerant vegetation in small sections of the lakebed (McKenna Neuman et al., 2018; National, 2020).

Due to these mitigation efforts, dust concentrations have significantly decreased, as for example, in 2018 the 24-hour maximum was 700 $\mu g/m^3$ (National, 2020). However, aquifers are a finite supply and precipitation is highly variable in the Owens Lake basin, which creates a challenge for dust management and affects water availability for California (National, 2020). Climate change is expected to greatly impact this water supply and therefore dust

controlling efforts, with longer and more severe droughts reducing the amount of water available to export from the aqueduct to control dust at Owens Lake (National, 2020). Rising temperatures will increase evaporation at Owens Lake, increasing the demand for water used for dust control, putting more pressure on the system, and creating a need to develop new mitigation approaches that use less water and maximize other environmental benefits (National, 2020).

1.3 Modes of Transport: Saltation and Breakdown

Bagnold (1941) identified three modes of aeolian particle transport, inclusive of suspension, saltation, and creep. Saltation is the focus of this study as it generally is the predominant mode of transport contributing to erosion in aeolian systems, provided there is a supply of sand sized particles within the bed; it is defined as the hopping motion of sand-sized particles along a surface which can initiate dust transport through bombardment of the surface (Shao, 1993). As stated by Gillette (1981), bombardment of the surface is responsible for most dust entrainment rather than entrainment by aerodynamic lift because of the cohesion created by interparticle forces. Based on these modes, there are various explanations for the mechanisms that underpin dust production in dryland regions. Alfaro and Gomes's (2001) suggest that the magnitude of dust emission is related to the kinetic energy of particles that move by saltation. Shao (1993) builds on this concept in suggesting that as saltating particles increase in energy they break down more substantially, thus producing more dust (Shao, 2001; Shao, 2004). Kok's (2011) brittle fragmentation theory similarly assumes that dust is produced by the breakdown of soil aggregates, where an aggregate is a group of primary soil particles that cohere to each other more strongly than to other surrounding particles (Tatarko, 2001; Fig. 1.1). The main binding agents affecting inter-particle cohesion are soil organic matter and clay minerals. However, if the forces associated with particle impact or rolling along the bed

surface are sufficient to overcome cohesion, aggregate breakdown and dust release may occur. PM_{10} emission is well recognized to increase with higher silt (<50 µm) and clay (< 2 µm) contents (Shao, 1993). In general, soils with PM_{10} tend to produce more dust, but only if the PM_{10} is released during saltation (Shao, 1993). This means that an increase in the saltation rate should lead to an increase in PM_{10} emission. However, many details concerning dust release during aeolian transport remain unknown, and in particular, need to be quantified as a basis for the development, validation and calibration of improved PM_{10} emission models.

Wind tunnel facilities have played a pivotal role in the simulation and study of the physics of saltation through providing a 1:1 scale model of a natural system that is easily manipulated. It is common in such experiments (O'Brien and McKenna Neuman, 2012; Langston and McKenna Neuman, 2005; McKenna Neuman and Maxwell, 1999; and McKenna Neuman and Maljiaars, 1997) to use a sand feed to seed saltation and reduce the fetch required to develop a saturated particle cloud. Simulation of saltation in wind tunnel settings is complimentary to observations made in the field and can reproduce or constrain saltation with a high degree of control, allowing detailed measurement of the aeolian transport process.

1.4 Aggregate Structure and Inter-Particle Force

Aggregation occurs when soil primary particles (sand, silt, and clay) are cohered together more strongly than with other surrounding particles (Nimmo, 2013). Not only does aggregation influence dust emission, but aggregation also influences micro and macro porosity, and thereby, drainage/aeration (Rieke et al., 2022). In macro pores, air and water can move freely, whereas in micro pores, the movement of air and water is slower and restricted. Larger aggregates preferentially form more macro pores while clay aggregates

form micro pores; therefore, the size and density of the aggregates present is also important to consider in regard to soil health (Rieke et al, 2022). Crop growth can be constrained by poor root development, slow water infiltration, and poor soil aeration, all of which are associated with poor soil porosity (Rieke et al., 2022).

The strength of the interparticle cohesion developed between soil particles depends on a variety of soil physical, chemical, and biological influences (Nimmo, 2013); as for example, texture (clay), water content and organic matter (Nimmo, 2013). An aggregate can vary considerably in diameter with macroaggregates ranging between 200 µm to 2000 µm and microaggregates falling under < 200 µm (Puget et al., 2000).

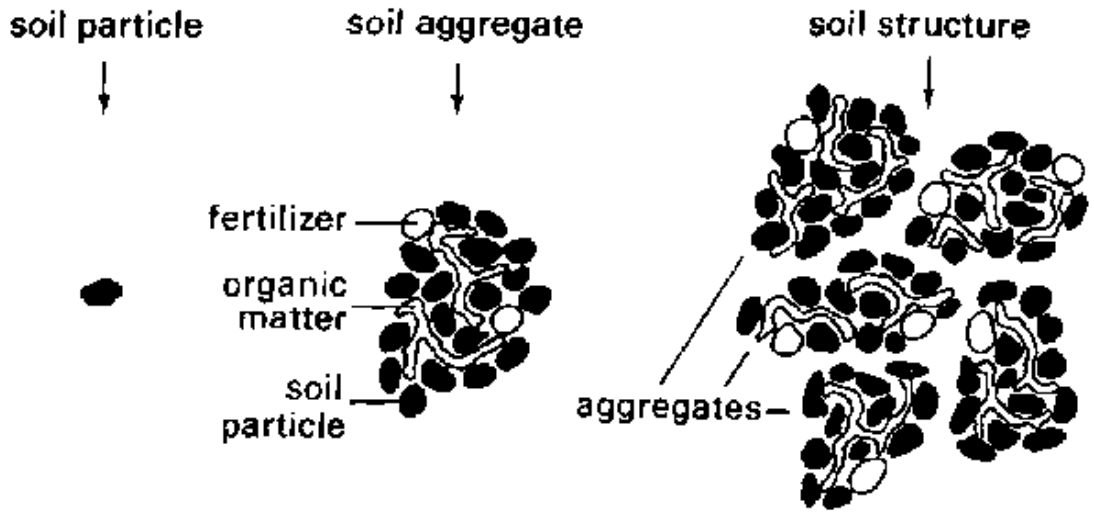

Figure 1.1. Illustration of an aggregate bound together by organic matter (Brouwer et al., 1985).

The resistance of such aggregates to breakdown with the application of external forces arising from saltation is measured as the dry aggregate stability (Tatarko, 2001). Aggregates with low stability break down more easily than aggregates with high aggregate stability (Tatarko, 2001). The stability of these aggregates is contingent on the interparticle forces that bind

them together. These not only affect the stability of the aggregates, but they also affect the susceptibility of a soil to entrainment by either impact or fluid drag (Fig. 1.2).

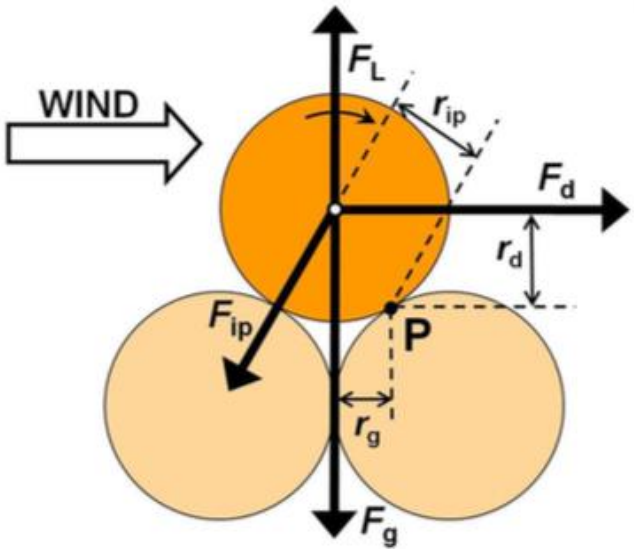

Figure 1.2. A diagram of the forces affecting particle entrainment with F_L being lift force, F_d being drag force, F_{ip} being interparticle force, F_g being gravitational force (Kok et al., 2012).

Fig. 1.2 depicts the forces that affect particle entrainment, including interparticle forces (F_{ip}). Under arid conditions without bulk pore water, the pressure potential is negative relative to atmospheric, also known as the matric potential (ψ), which affects both capillary and adsorptive force (McKenna Neuman and Sanderson, 2008). Adsorbed water within soils increases the cohesion between particles adjacent to each other, resisting the fluid drag of the wind (McKenna Neuman, 2003). The cohesive force is directly proportional to the matric potential, and the area of contact between the adsorbed water (McKenna Neuman, 2003). Although matric potential decreases as the water content increases (Fig. 1.3), the contact area expands at a higher rate, resulting in a large amount of cohesion (McKenna Neuman, 2003).

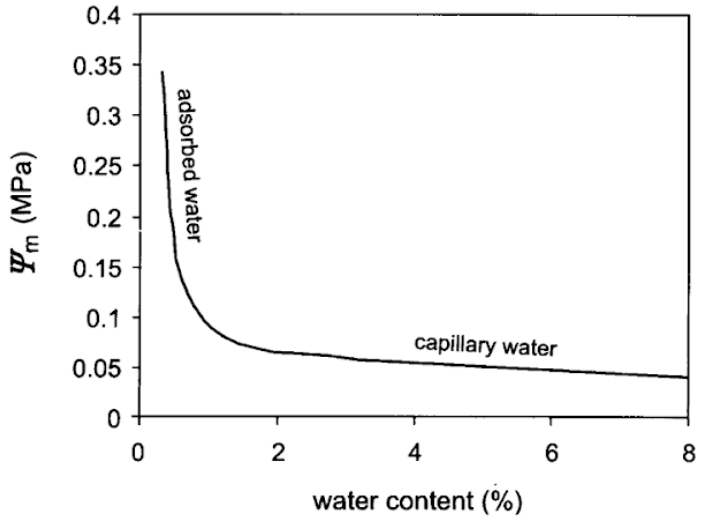

Figure 1.3. Sorption curve for medium sand demonstrating the matric potential decreases very slowly below 0.1 MPa, but with continued drying increases very rapidly above 0.2 MPa (McKenna Neuman, 2003).

The tension at which water is adsorbed onto the surfaces of mineral particles (ψ) varies with the humidity and temperature of air within the soil voids. When a completely dry soil is exposed to an atmosphere with relative humidity between 35% and 40%, a single layer of water is adsorbed onto the surface by hydrogen bonding (McKenna Neuman and Sanderson, 2008). This water is held in place by very strong forces and has a thickness of approximately 0.3 nm (McKenna Neuman and Sanderson, 2008). As the relative humidity increases, additional water is adsorbed, with a second layer adsorbed at about 60% relative humidity (McKenna Neuman and Sanderson, 2008). Therefore, by increasing the humidity, the strength of the tension will increase, thereby increasing the strength of the interparticle force. McKenna Neuman (2003) summarizes the potential influence of climate upon the entrainment of particles (Fig. 1.4).

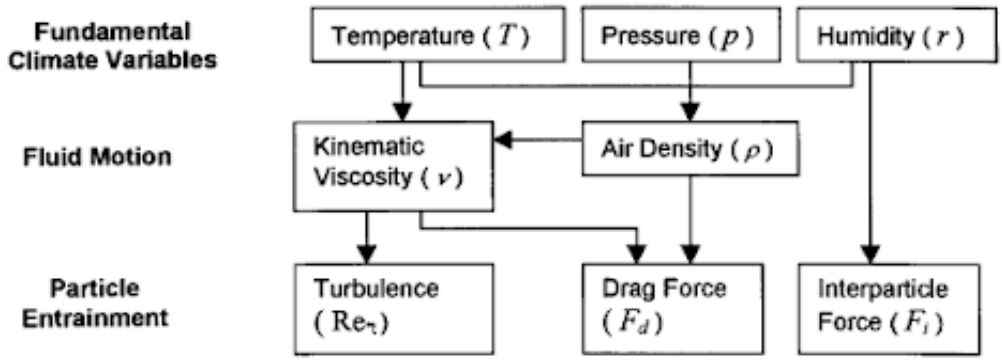

Figure 1.4. A flow diagram of the effect of different climate variables on particle entrainment (McKenna Neuman, 2003).

Thus, in arid regions, surface soil moisture can be significantly affected by changes in atmospheric humidity, with important effects on aggregate entrainment and break down. In the context of Owens Lake, surface moisture can be added through either precipitation or capillary rise and lost through evaporation or percolation. As wind blows over the damp, unvegetated surface, the top layer of sediment will completely dry over time, if the evaporated water is not resupplied. When the fluid drag just exceeds the particle weight and cohesive force, also known as threshold friction velocity (u_{*t}), entrainment will occur. Given that Owens Lake can reach relative humidities up to 50%, adsorbed water can be resupplied between particles in an aggregate, thereby promoting its resistance to break down and dust production. Quantification of the dust production efficiency under varying humidity is needed, as no measurements currently exist.

In the context of this study, chemical influences on interparticle cohesion are regarded as being most important, inclusive of cementation by precipitated solutes, such as salt, among other minerals (Nimmo, 2013). A salt is a product of the reaction of an acid and a base where the H of the acid is replaced with the cation of the base. In the context of Owens Lake, saline

groundwater containing soluble ions such as K+, Ca2+, Cl-, or Ma2+ can percolate through the sediment and evaporate in the pore spaces, so that the evaporate minerals may lightly cement other grains (Nield et al., 2016). Cations that are not Na+ help promote aggregation via cation bridging between clays, with the precipitates acting as a chemical cement. Saline soils primarily impact plant health via osmotic stress. A saline soil has an electrical conductivity (EC) of >4000 uS/cm in a saturated paste. In contrast, sodic groundwater is more problematic as it contains high levels of Na+, which can leach through the soil and weaken the bond between soil particles (Nimmo, 2013). The forces that hold clay particles together are weakened when excessive sodium is adsorbed at the negatively charged surface of clay particles (Nimmo, 2013). The extent of soil sodicity is measured either through the Exchangeable Sodium Percentage (ESP) or Sodium Adsorption Ratio (SAR). These indices quantify the sodium content of sediment in relation to calcium and magnesium. A soil is interpreted as sodic if it has an ESP of >15 or an SAR of >13, dispersion of the soil particles occurs leading to destruction of the soil structure.

It is important to distinguish whether the sediments at Owens Lake are sodic or saline, given the implications for aggregate stability. Sodic soils are weak as a result of the weak soil structure, although the dispersed clays can block voids, limiting drainage and increasing the risk of water erosion. They can also limit root penetration and vegetation establishment which offer important protection from wind erosion and add organic acids (cements) to the sediment. Salt crusts are common on Owens Lake as a result of saline or sodic groundwater penetration and high evaporation. Both mechanical and chemical processes operating on a playa can degrade the salt crust surface, resulting in a brittle physical state (Nield et al., 2016). A sodic crust has greater potential to be more emissive than a saline crust, as a result of the weak and disruptive bonding. Other typical cementing agents that can precipitate

include calcium carbonate (Nimmo, 2013). Therefore, knowledge of the minerals that constitute the aggregates formed within the sediment from Owens Lake can provide some indication of the relative strength of the interparticle forces that bind them.

1.5 Dust Suspension, Dispersion, and Settling

Dust suspension is a result of three main mechanisms: aerodynamic lift, saltation bombardment, and aggregate disintegration (Shao, 2008). Aerodynamic lift is the entrainment of dust by wind when drag exceeds the gravitational force (Shao, 2008). Saltation bombardment occurs when saltating particles impact a surface of dust, ejecting them from the surface (Shao, 2008). Numerous works (Gordon and McKenna Neuman, 2009) have suggested that saltation of sand sized aggregates may rapidly abrade to release dust that then enters suspension. Lastly, aggregate disintegration occurs when dust is removed from the surface of an aggregate due to impact with the surface, or when an aggregate breaks down as a result of an impact on the surface, releasing dust particles in the process (Shao, 2008). Kinetic energy transferred to the bed surface from impact can cause a rupture of a crust or aggregate (Gordon and McKenna Neuman, 2009). In the case of silt sized particles (< 63 μm), the interparticle force proportionally gains importance relative to the drag force, thus making dust more difficult to entrain solely through wind drag. As the particle size decreases, aerodynamic forces become negligible and cohesive forces dominate, restricting the supply of grains to the air stream from bonded surfaces. However, bombardment by saltating particles or aggregate disintegration can easily disrupt these cohesive forces and so allow dust entrainment.

In these dust supply limited systems, the threshold shear velocity is increased with the contribution of particles to the airstream being below the transport capacity of the wind

(Nickling and Neuman, 1995). The shear or friction velocity ($u*$) in a boundary-layer flow is described by the law of the wall (E1),

$$u* = \frac{ku_z}{ln}\left(\frac{z}{z_o}\right) \qquad (E1)$$

in which k is the von Karman constant with a value of ~0.41, z is elevation in m, z_o is aerodynamic roughness height in m, and u_z is horizontal velocity at a given elevation in ms^{-1}. Once in suspension, dust is transported locally from the surface by two mechanisms: horizontal advection and turbulent diffusion, which governs the transport of mass, heat, or momentum within a system (Roney and White, 2006). Dust particles finer than 20 μm are transported mainly in long-term suspension over a great height range and may be widely dispersed (Wang et al., 2008). The size of a grain determines not only the distance over which the grain is transported, but also its transport height, its response to turbulence, and the amount of energy carried by the particle during its transport (Wang et al., 2008). Gravity opposes this motion, so that the suspended dust particles will eventually descend towards the ground in accordance with their size (Xiao and Taylor, 2002). Gravitational settling tends to make the particle drift decrease with height, whereas turbulent diffusion results in a uniform vertical particle distribution (Xiao and Taylor, 2002).

Surface roughness is a factor that has the potential to influence dust suspension and settling. Surface roughness is a defining feature of high turbulence flows (Bhaganagar et al., 2004). The higher the Reynolds number, i.e., higher turbulence, the more likely the effects of roughness are significant (Bhaganagar et al., 2004). However, the effects of surface roughness on turbulence are not entirely understood. The turbulent boundary-layer over a rough surface contains a roughness sublayer, where the flow is directly influenced by individual roughness elements and is not spatially homogenous (Bhaganagar et al., 2004). In

the context of dust suspension and settling, an increase in surface roughness has the potential to increase turbulence intensity and shear stress on the bed surface, which can in part enhance the suspension of dust particles. Therefore, in this study, the effect of dispersion and settling on both the vertical and horizontal dust flux as a result of aggregate disintegration of Owens Lake sediments is thoroughly explored with surface roughness as an influencing factor.

1.6 Research Questions and Objectives

This project has two independent goals. The first is to observe and quanitify aggregate disintegration during saltation. The second goal is to assess the dispersion of dust generated during the saltation of sediments collected from Owens Lake playa. Relative humidity, windspeed, and surface roughness were varied during the experiments. This project tested the following hypotheses:

i) Aggregate particle diameter decreases linearly with increasing distance of transport.

ii) Rougher bed surfaces enhance the rate of aggregate disintegration with distance of travel.

iii) Dust production increases exponentially with increasing distance of transport.

iv) Dust dispersion is enhanced by increasing surface roughness.

To test these hypotheses, experiments were carried out in a boundary-layer wind tunnel in which a fixed amount of 500 μm aggregates were blown through the working section of the wind tunnel under varied conditions of surface roughness, wind speed, and humidity. Their disintegration through abrasion was measured optically after capturing them on microscope slides that were coated with glycerol and mounted on the floor of the wind tunnel. The concentration of dust in dispersion plume was measured using DustTraks, with the

dispersion plume experiments. A set of references experiment was run in which 63 μm silt particles replaced the aggregates introduced through the drop tube. X-ray Diffraction and Scanning Electron Microscopy (SEM) were used to characterize the geochemistry/mineralogy of the Owens Lake sediments and the structure of the particle aggregates, respectively.

Chapter Two: Methods

2.1 Overview of General Methodology

The overarching goals of the project were addressed in a wind tunnel simulation in which sediment collected from Owens Lake was blown through the working section of the wind tunnel and the dust concentration, aggregate disintegration, and particle speed were measured under varying wind speeds and relative humidities. An attempt to profile the flow structure of the working section of the tunnel was also made in this simulation. In support of these experiments, various properties of the Owens Lake sediment were assessed in the laboratory, inclusive of their particle size distribution, aggregate density, pH, conductivity, mineral composition, and physical structure.

2.2 Sediment Processing and Analysis

2.2.1 Context

Owens Lake is the terminal lake of what was originally known as Owens River (Fig. 2.1), at the south end of the Owens Valley (Gill and Cahill, 1992). The most recent desiccation of Owens Lake resulted in a dried lakebed with an area of approximately 280 km^2 (Gill and Cahill, 1992).

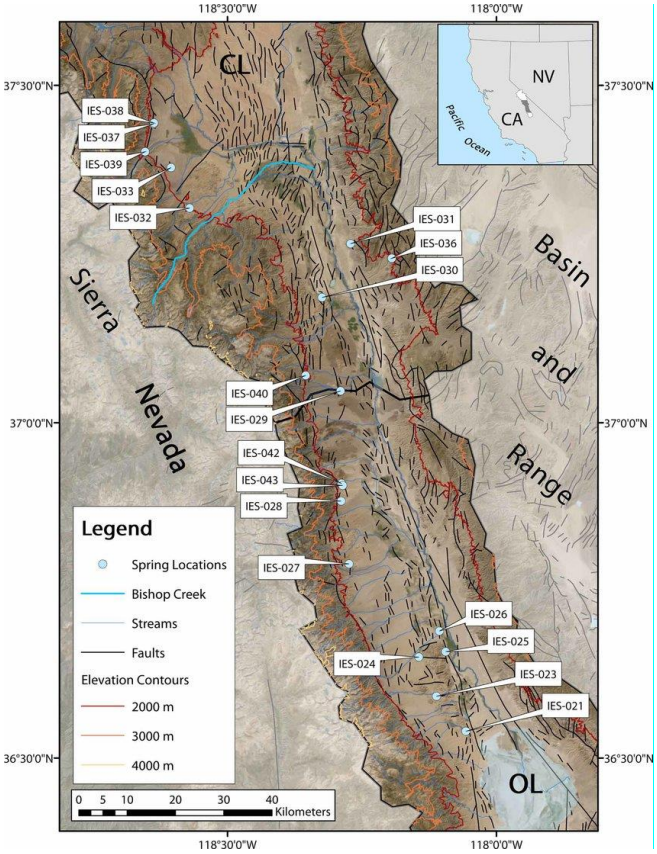

Figure 2.1. Inset map of Owens Lake (OL) watershed including the Crowley Lake (CL) sub watershed, with the location of Owens Lake and River indicated in the top right (Meyers et al., 2021).

Bulk surface samples of Owens Lake sediment were collected for an earlier study at different locations on the dry lakebed by Air Sciences Inc. field staff and W. G. Nickling and shipped to Trent University in Peterborough, Ontario, Canada. The goal of this study was to identify the range of water saturation in which an acceptable level of dust control can be obtained. The main material used in this thesis study was the finest textured sediment (0.1-1000 µm) referred to as T10 by McKenna Neuman et al., 2018. T10 was used rather than T26 (100-1000µm) which has a higher salt content. McKenna Neuman et al., (2018) previously characterized the T10 sediments on Owen's Lake using a Horiba LA-950V2 to measure the

range in particle diameter. The particle distribution results are reported in Fig. 2.2, respectively.

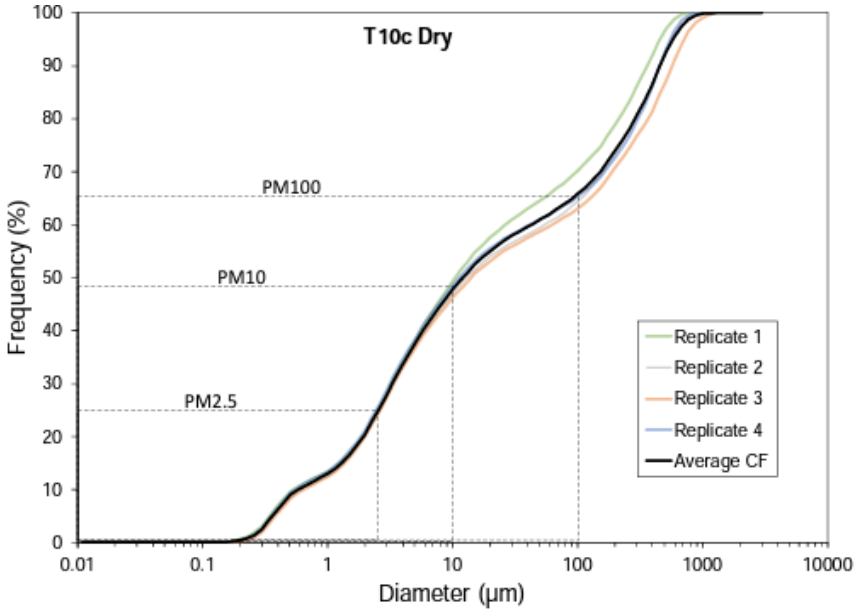

Figure 2.2. Cumulative frequency distribution of particle diameter for sample T10 replicate c dry (source: McKenna Neuman et al., 2018).

Measurements of the bulk density, pH, water, and salt content carried out by McKenna Neuman et al., (2018) are also reported in Table 2.1.

Table 2.1. Summary of physical properties for replicates a through d measured for the T10 sediment at Owens Lake (source: McKenna Neuman et al., 2018).

Sample Name	*Bulk Density (g/cm³)*	*Moisture Content (%)*	*pH*	*Conductivity (mS/cm)*
T10b Dry	1.17	19.1	10.58	18.77
T10c Dry	1.23	19.7	10.76	17.64
T10d Dry	1.19	17.7	10.59	16.56
Average	**1.18**	**19.1**	**10.58**	**17.98**

Though it was not measured in this study, an attempt to measure the SAR, among other properties, was made by Chadwick et al., (2006) for samples collected from the northern area of Owens Lake playa. The results are presented in Table 2.2.

Table 2.2. Summary of physical properties of test samples at an experimental site.

Experimental Site	SAR	pH	EC (uS/cm)
Pit 1 and 2	12.5-21.3	>8.5	250-1100

Further details regarding the geomorphic history of the region, methodology, soil characteristics, as well as human history can be found in the following publications: McKenna Neuman et al., (2018), Gillette et al., (1997), Gill and Cahill (1992), Gill and Gillette (1991), Font (1995), and Reheis (1997).

2.2.2 Particle Size Distribution

Two size classes for the T10 sediment, a disaggregated sample with a maximum diameter in the silt size range (≤ 63 µm) and an aggregated sample with a minimum diameter in the sand size range (≥ 500 µm), were selected for the wind tunnel experiments (Fig. 2.3). A particle diameter of 63 µm was chosen as a reference to address the second objective in measuring the dispersion regime associated with a plume of fully suspended particles in the absence of saltation and a secondary source of dust production, i.e., aggregate breakdown. To ensure the silt particles were disaggregated, they were pulverized with a mortar and pestle before any experiments were conducted. The 500 µm particle aggregates address the first, second, and third hypotheses listed in Ch 1, in tracking aggregate breakdown and characterizing the dispersion regime with saltation. In pilot testing, 500 µm aggregates were determined to be the optimal average aggregate size to produce detectable dust concentrations within the

dispersion plume, but not so large as to overload the DustTraks. Larger aggregates were unable to saltate and produce dust, unless under extreme wind speeds > 11 ms^{-1} in the TEWT laboratory facility.

To isolate each of the desired size classes, particles were sieved by hand, where the aggregates were retained on the 500 µm sieve to achieve a minimum diameter of 500 µm and maximum of 710 µm, while the silt particles passed through the 63 µm sieve to obtain a maximum diameter of 63 µm. However, 500 µm aggregates were in finite supply in the relatively fine textured T10 sediment provided by the Air Sciences field team. Therefore, additional aggregates had to be created from this sediment to have enough for the wind tunnel experiments. To do this, the T10 sediment was placed in trays, wetted and then dried, so that it formed cohesive bricks. The material was then placed in a concrete mixer with large limestone cobbles, and with the tumbling, the bricks fractured into smaller units from which 500 µm aggregates extracted by sieving. There are errors associated with this method as abrasion of both the paint within the concrete mixer and the limestone cobbles the potentially contaminated the samples.

To confirm the particle diameter and accuracy of hand sieving, subsamples of the 500 µm aggregates and 63 µm particles were reserved for the Horiba LA-950V2 laser scattering particle size distribution analyzer. In addition to agitation and circulation within the instrument, a Calgon solution was added to enhance dispersion. The particle size distribution for both the 63 µm silt particles and 500 µm aggregates was sampled three times and averaged (Fig. 2.3). There was no attempt to determine the particle size distribution of disaggregated 500 µm samples. Therefore, we cannot distinguish between a grain that is 500

µm, or an aggregate that is 500 µm for the wind tunnel experiments, but the term aggregate was chosen as the general terminology for this size class.

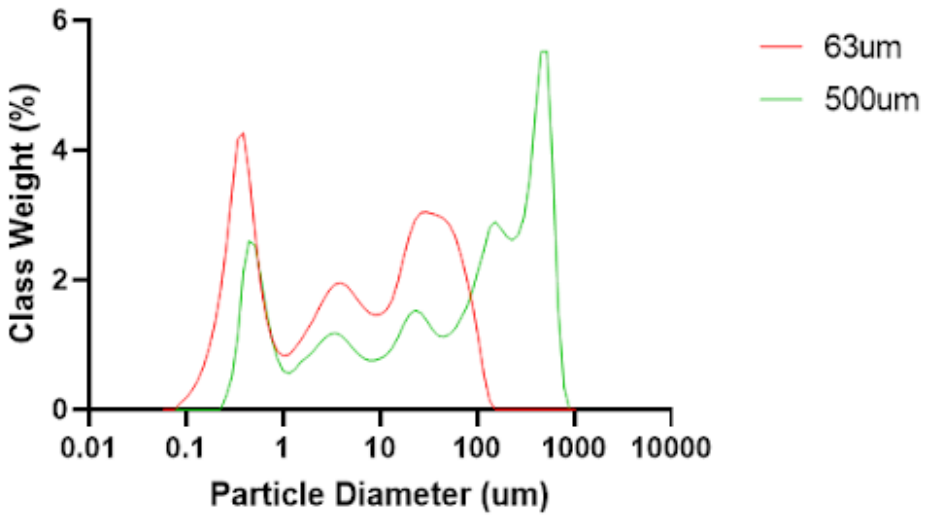

Figure 2.3. Average particle distribution using the Horiba™ of 500 and 63 µm aggregates, showing a total of 64% sand, 25% silt, and 18% clay for 500 µm and a total of 30% sand, 48% silt, and 39% clay for 63 µm.

The distribution for both is multimodal and poorly sorted, which in part might be attributed to uncertainties associated with measuring the particle distribution with the Horiba. This instrument analyzes suspensions, so the salts that cemented the aggregates would have dissolved to some degree and thereby skewed the results toward the fine tail. Despite the errors associated with hand sieving non-spherical particles (i.e. the effect of orientation for oblong particles relative to the mesh opening), this method was determined as adequate for achieving an approximate particle size for the experiments.

2.2.3 Physical Property Analysis

Conductivity and pH were measured using the Fisher Scientific™ Accumet AP75 probe. The probe was calibrated prior to use, and given the extreme salt content and pH, as shown in

Table 2.2, the highest standard available was used for calibration, specifically the 1413µS/cm standard. The solid: solution ratio used to measure the pH and conductivity was 1:2; specifically, 10 g of the sample were added to 20 mL of deionized water, then the probe was swirled in the slurry over a period of 5 min for the suspension to reach equilibrium. The pH was also calibrated using a 7 and 10 standard for a two-point calibration.

Aggregate density was calculated by first measuring the mass of ten discreet 500 µm aggregates using a scale with a precision of 10^{-4} g. The value obtained was divided by ten to determine the mass of a single aggregate. The volume was then approximated by the spherical equivalent using the following equation (E2),

$$V = \frac{4}{3}\pi\left(\frac{d}{2}\right)^3 \qquad (E2)$$

where π is 3.14 and d is the aggregate diameter. A density of 1.32 g/cm^3 was then obtained from dividing the mass by the volume. The low value, about half that of quartz, confirms that the particles were indeed aggregates of smaller particles and not a solid sand grain.

Table 2.3. Summary of the physical properties of the T10 sediment from Owen's Lake.

Sample	Aggregate Density (g/cm³)	pH	EC (uS/cm)
T10	1.32	9.67	4150

The salts and minerals in the samples were characterized using powdered XRD at Trent University in the Environmental Geochemistry Laboratory. XRD was used to determine the mineral composition from the peak positions and intensities within the sampled diffraction pattern. This technique reveals the fundamental physical properties of the material, and also

helps in identifying not only the material itself, but elucidates its structure (Selva et al., 2021). A mortar and pestle were used to pulverize the sediment before mounting it into the XRD. Sample powder was mounted in the front-loading holder and a diffraction pattern was collected using a Bruker D2 Phaser diffractometer with a 0.02 step size over a range of 5–80° 2θ at 2 s/step with a 15-rpm spin (Bruker, 2008). Mineral phase identification was conducted using search-match software, DIFFRACplus EVA 14 (Bruker, 2008) and crystal structure data from the International Center for Diffraction Data PDF 2+ 2010. One replicate was completed for the T10 sediment sample.

Lastly, the morphology of selected aggregates was analyzed using Scanning Electron Microscopy (JSM-7800F Field Emission SEM with 5 kV electron accelerating voltage) by Dr. Joanna Bullard at the Materials Science lab at Loughborough University UK. All samples were coated with gold/palladium before the analysis to limit surface charging.

2.3 Wind Tunnel Facility and Instrumentation

2.3.1 Wind Tunnel Facility

The Trent University Environmental Wind Tunnel (TEWT, Fig. 2.4) is a relatively low speed research facility that is designed to simulate the atmospheric boundary layer both in clear air and with particle transport (McKenna Neuman, 2016). It is an example of an open-loop system, where the intake and outlet of the tunnel are not connected (McKenna Neuman, 2016). An advantage of this design is that the intake air is clean or devoid of particles. The wind tunnel's main features are that it has temperature control, with the ability to be chilled as low as -15°C; the wind speed is precisely controlled and can reach up to 18 ms^{-1}; and there is full humidity control from 5% to 95% (McKenna Neuman, 2016). The wind tunnel working section is 12 m long, with a cross sectional area of 0.71 m x 0.72 m, in which necessary instruments were mounted along this working section for experimental measurements.

Figure 2.4. Image of the TEWT.

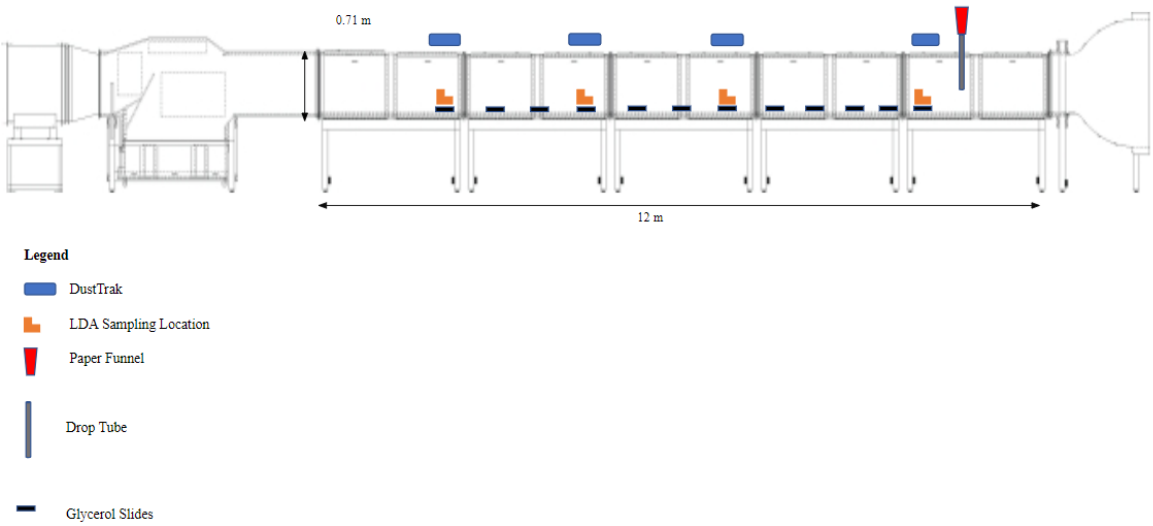

Figure 2.5. Diagram of the wind tunnel set up for the experimental design to address how aggregate dynamics affect dust generation.

2.3.2 Instrumentation

The concentration of dust released in the wind tunnel experiments with abrasion of the aggregates was measured with a TSI™ DustTrak Aerosol Monitor. The DustTrak uses an

external pump to suck in air with a flow rate of 1 L/min. The DustTrak monitor then uses a light-scattering laser photometer that provides real-time aerosol mass readings (PM_{10} concentration) and can collect a gravimetric sample (TSI, 2021). They combine both particle cloud (total area of scattered light) and single particle detection to achieve mass fraction measurements (TSI, 2021). It uses a sheath air system that isolates the aerosol in the optics chamber to keep the optics clean for improved reliability and low maintenance (TSI, 2021).

A Dantec 2D Laser Doppler Anemometer (LDA) was used to measure the velocity components of the sediment particles moving in saltation as well as that of neutrally buoyant traces moving within the airflow. The instrument generates two visible (wavelength $\lambda = 0.660$ μm) and two invisible ($\lambda = 0.785$ μm) laser beams that intersect in a 0.04 mm^2 sampling volume (Dantec, 2021). When a given particle passes through the sampling volume, the fringe interference is processed to obtain the horizontal and vertical velocity components (Dantec, 2021). The location of the LDA sampling volume is controlled by a programmable 2-D traverse allowing horizontal and vertical coordinate positioning. Sampling of the flow velocity within discrete planes at selected positions along a spanwise traverse can be achieved by manually moving the LDA system either toward or away from the centerline of the tunnel working section (McKenna Neuman and Bedard, 2015).

A Motic BA310E scope was used to take pictures of the microscope slides coated with glycerol, referred to as glycerol slides. The images were subsequently analysed using a custom written MATLAB program to quantify the amount of aggregate fining with fetch. The microscope provides maximum illumination quality to distinguish between intact and fragmented aggregates and reveal the size characteristics of each. The distance between the tube lens and objective is fixed at 160 mm to allow for other optical components to be inserted between the objective and tube head (Motic, n.d.).

2.4 Experimental Design

2.4.1 Wind Tunnel Simulation

The freestream wind speeds selected for the experiments were 8, 10, and 11 ms^{-1} with a constant temperature of 20°C, varied relative humidity at 20%, 35%, and 50%, and varied surface roughness (smooth versus rough floor). Owen's Lake temperature, wind speed, and relative humidity vary substantially throughout the year. In the winter months, relative humidity is on average 50%, whereas in the summer months, relative humidity is on average 20%, with an annual average of 30%, thus giving the rationale behind the values chosen for the relative humidity (US, 2022). However, due to the time constraints in adding another variable, a constant value for temperature was chosen based on the average annual temperature in Owen's Lake, being 20°C (US, 2022). Lastly, the chosen wind speeds for the simulation were 8, 10 and 11ms^{-1} for the smooth floorboards, and 10 and 11 ms^{-1} for the rough floorboards. These wind speeds were established after pilot testing confirmed that they exceeded the threshold required for sustained particle motion for each surface type. The pilot testing was conducted by dropping the aggregates into the wind tunnel via a drop tube, with wind speeds starting at 4 ms^{-1}, and increasing by 0.25 ms^{-1} until the aggregates were able to saltate. From this, the threshold for saltation was determined to be 8 ms^{-1} for the smooth floor and 10 ms^{-1} for the rough floor. This further explains the rationale behind not measuring dust production at 8 ms^{-1} over the rough floor, though this wind speed is used for the smooth floor experiments.

With regard to Owen's Lake, the average annual wind speed is 3 ms^{-1}; however, extreme wind events in the Owen's Valley are a very common phenomenon so that dust emissions events can exceed human health standards. The 24-hour average PM_{10} concentrations can exceed 12,000 $\mu g/m^3$, which is more than 75 times the federal PM_{10} standard (Ono et al.,

2011). Wind speeds common during these events typically exceed 18 ms^{-1} at 10 m elevation (Zhong et al. 2008). The equivalent speed in the freestream of the TEWT is 14 ms^{-1}, although at this rate, fine grains of sand can enter intermittent suspension and strike the tunnel roof. Cahill et al. (1996) report that field measurements of PM10 concentrations near the Owens playa exceeded 27,000 $\mu g/m^3$ during a 10-minute storm period in a wind speed of 11 ms^{-1} in the spring of 1993, equivalent to 8.7 m s^{-1} in TEWT assuming similar friction velocity and aerodynamic roughness.

Lastly, the rationale behind using a smooth and a rough floor for these experiments is to determine the effect on aggregate breakdown and dust production. The rough floor was composed of plywood plates with coarse sand glued to them to add increase surface texture, whereas the plates comprising the smooth floor were sanded and varnished.

In the context of the experiment, a fixed mass of particle aggregates (20 g) was delivered by a gravity feed to the wind tunnel through a short metal tube that was grounded to minimize static electricity and prevent the particles from sticking to the tube or one another. A non-conductive funnel was created in-house out of craft paper to also reduce static electricity (Fig. 2.6). The bottom of the tube was positioned 0.2 m above the bed surface and 0.8 m downwind of the trip plate. Fig. 2.6 illustrates the sediment delivery apparatus.

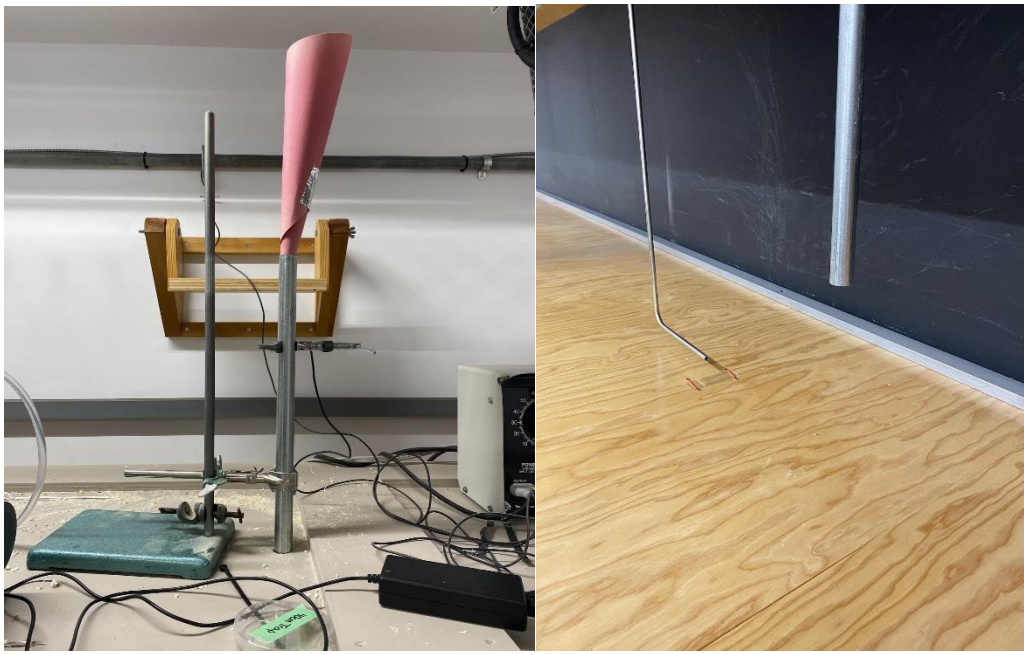

Figure 2.6. Left: Funnel made of construction paper attached to the top of the drop tube. Right: Grounded sediment delivery tube with outlet positioned 0.2 m above the bed of the wind tunnel.

The particle aggregates delivered through the drop tube impacted a non-emissive surface below. This method was used to isolate dust produced from the fracture of isolated particle aggregates following an impact, as opposed to bombarding aggregates present within a bed surface with saltating sand particles wherein the exact origin of the dust source would be difficult to identify. Specifically, both the aggregates and sand feed particles would have been collected on the glycerol slides, and since all sand bears a small fraction of dust, it would have contributed to that released from the aggregates. Furthermore, fluid drag alone is generally not sufficient to entrain 500 μm aggregates unless under extreme wind speeds. The initiation of motion usually arises from the impact of a particle travelling in saltation, but in this case, the impact force needed to eject the aggregate into a ballistic trajectory was delivered in a more controlled manner. To verify that a fraction of the 500 μm samples could not emit PM10 in the absence of an impact, pilot testing was conducted in which aggregates

were placed in the wind tunnel at a speed at which the aggregates could not saltate. The aggregates without abrasion or saltation did not produce any dust.

The purpose of the first set of experiments was to characterize the emissions of PM_{10} with abrasion of the 500 µm aggregates during their transport at varying wind speeds of 8, 10, and 11 ms^{-1} with varying relative humidities at 20, 35, and 50% and a constant air temperature of 20 °C. DustTrak™ II aerosol monitors were used to measure PM_{10} concentration associated with fracture of the particle aggregates during their transport in the airstream. The intake tube of each of four DustTrak monitors was mounted from the roof of the wind tunnel positioned at 0.3, 3.71, 5.94 and 8.33 m downwind from the drop tube. All four DustTraks were cross-referenced with each other to confirm that the background PM concentration was consistent along the working section of the wind tunnel before the start of each experiment. Each DustTrak was also cleaned and calibrated before each test to decrease noise in the results and improve accuracy. The DustTraks were calibrated by first cleaning out the filters, and then placing a PM2.5 impactor tube at the intake and pulling in clean air for 60 seconds.

The experimental design involved sampling a vertical profile of the dust dispersion plume created by the fracture of 20 g of 500 µm aggregates. The mass dropped down the tube was considered an optimal amount after various pilot tests confirmed than an amount less than 20 g was not sufficient for PM_{10} detection, while more than 20 g saturated the DustTrak. The fixed amount of aggregate inserted was necessary to normalize the PM_{10} concentration values in order to remove the effect of variable aggregate delivery. At each downwind position (Fig. 2.5), the dust concentration was sampled at an elevation of 0.02, 0.035, 0.05, 0.075, 0.1, 0.125, and 0.15 m over a total of 3 replicate experiments lasting 30 seconds each.

To capture a subsample of the aggregates for measuring their disintegration downwind, 12 glass slides coated with sticky glycerol and mounted with elastics and nails were co-located with each DustTrak, as well as placed between them for each experiment (Fig. 2.5; Fig. 2.7). These experiments were replicated 3 times, so that in total 540 glass slides were obtained. Rolling or saltating particles that landed on these traps stuck to the surface, however, the sample area (1 cm^2) of the glycerol trap at each downwind location was low relative to the width of the wind tunnel floor. When the experiment ended, each slide was removed and photographed in order to assess the number of particles captured and their size distribution. Photographs of the slides were obtained using a Motic BA310 Microscope at 10x/0.25 magnification. The images were later analyzed using a MATLAB program written specifically for this study (Fig. A1.1 and A1.2) by Dr. Patrick O'Brien. The program uses image analysis and area detection to determine the concentration of particles as the percentage of black (particle) to white (no particle) pixels (Fig. 2.8). This code also outputs the properties of the detected objects, inclusive of the area, perimeter, circularity, and longest axis, with the overall goal of determining particle diameter from these properties.

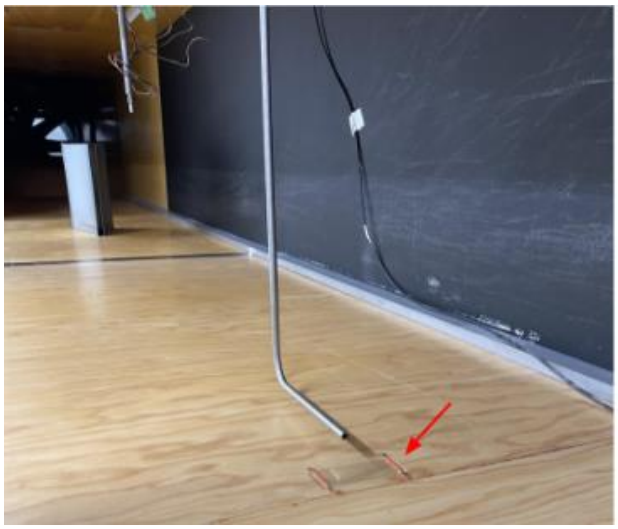

Figure 2.7. Co-located glycerol trap (indicated by red arrow) and dust intake tube.

a) 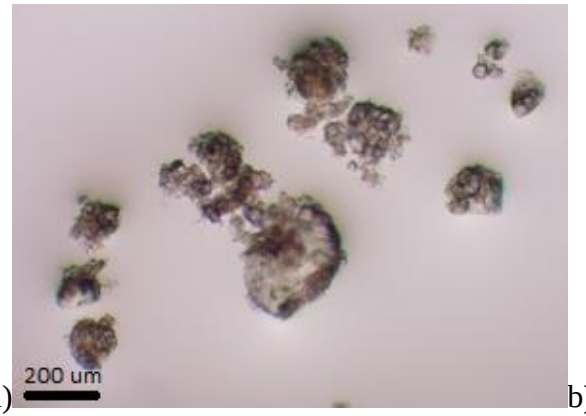

b) 

Figure 2.8. a) original image of a particles collected on a sample glycerol slide ; b) binary output after running the MATLAB program.

Lastly, a Dantec LDA Flow Explorer was used to sample particle speed and profile the boundary layer flow to obtain u_*. Since the shear within the flow strongly affects particle acceleration and the impact energy, friction velocity, u*, was calculated from u_p using the von Karman equation (E1). The particle speed experiments were repeated four times, with the LDA placed at different locations downwind (0.3, 3.71, 5.94, and 8.33 m; Fig. 2.6). At each location, the LDA sampled velocity in a vertical array at 0.02, 0.035, 0.05, 0.075, 0.1, 0.125, and 0.15 m relative to the bed of the tunnel, with a sampling time of 5 seconds at each elevation. The LDA has the capability to sample continuously along a pre-programmed vertical profile, therefore only one experiment needed to be conducted at each horizontal location. The LDA measures the speed of any particle moving through the intersection of its laser beams, inclusive of both 500 µm aggregates and dust. Unfortunately, we cannot distinguish between sampled mean velocities associated with the aggregate and dust particles. In this study, the particle velocity was measured at all 4 DustTrak locations (Fig. 2.5) over varying elevations and wind speeds. Since most saltating particles that are large move very close to the bed, well under 10 mm, the particle velocities sampled in this study were primarily associated with suspended dust released from the aggregates.

During pilot testing, the dust concentration trends measured at ≈ 6 and 8 m downwind of the drop tube appeared confusing. In a wall bounded flow, there can be vortical structures that affect the shear across the tunnel, both in terms of the streamwise and vertical component velocity. The vertical component, specifically, has implications for particle suspension and settling and any perturbation will affect the dust concentration. It therefore became necessary to fully characterize the airflow profile in cross section at both locations in order to better contextualize and interpret the dust concentration results.

This required LDA measurement throughout a plane oriented perpendicular to the mean flow (Fig. 2.9). The grid array was sampled every 2 cm in the Z direction starting in the middle of the tunnel (30 cm from the wind tunnel glass windows) and every 1.5 cm vertically starting at 2 cm from the bed and finishing 15 cm above the bed (Fig. 2.9). This grid was designed with a low density due to time constraints and the fact that the LDA cannot be manually moved spanwise across the width of the tunnel in small increments. The sampling volume of the LDA laser was first positioned in the middle of the wind tunnel and then moved towards the glass door. Because of geometric and hardware constraints, the LDA cannot measure all the way to the back wall. Thus, we must assume that the flow structure in the right half of the tunnel mirrors the left half that was measured. Before each set of measurements, the wind tunnel was filled with neutrally buoyant particles (glycerine-based fog) and the freestream wind speed set to 8 ms^{-1}. At each node in the grid array, the wind speed components were sampled for 30 seconds while only 1 replicate was completed for each point. The optimized settings for the Burst Spectrum Analyzer (BSA) Flow Explorer Processor are summarized in Table 2.4.

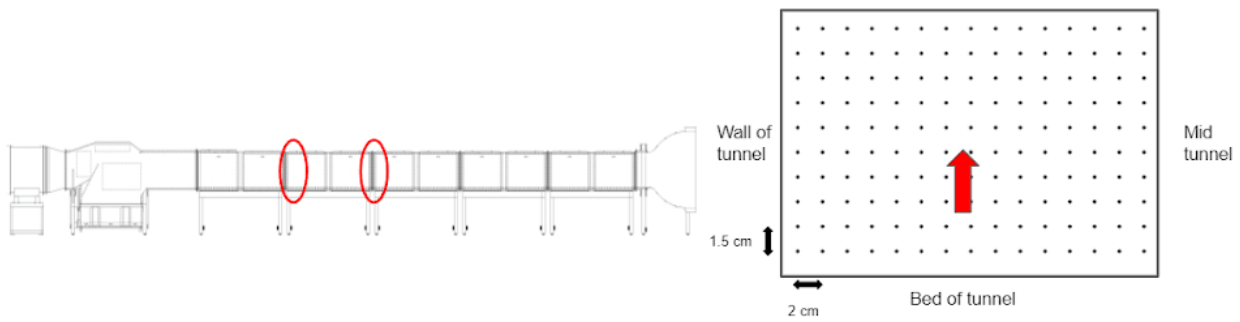

Figure 2.9. Left: Diagram illustrating positions of LDA for clean air grid profiling. Right: Sampling grid aligned perpendicular to the principal flow direction (horizontal).

Table 2.4. Summary table of the optimal LDA settings demonstrated to produce the least amount of noise within the measurement data.

	Settings
LDA 1 Sensitivity	1000 V
LDA 2 Sensitivity	1200 V
Record Length	128-256
Gain	18 dB
Validation	2

2.4.2 Reference Experiments

The aggregates introduced in the wind tunnel experiments were expected to break down through abrasion; that is, that the more the particles collide, the more they fracture, so that there a fining of particles downwind should be observed. However, as a result of the variation in particle speed and trajectory length with particle diameter, sorting and fining might also

have developed downwind for reasons that had nothing to do with particle fracture. In order to address the first hypothesis listed in Ch 1, a reference experiment was carried out with discrete or uncemented sand particles to isolate the natural fining of particles downwind from that associated with aggregate breakdown. The control sand had a mean diameter of approximately 500 µm (Fig. 2.10), similar to the nominal diameter of the particle aggregates, with a range between 200 µm and 1000 µm. Even though the control sand was strongly unimodal, sorting could have taken place provided the distance of transport was sufficient. The overarching rationale was that aggregate communition would only be supported by a downwind decrease in diameter exceeding that arising from the natural sorting of the sand particles. As shown in Fig. 2.5, the control experiment was set up very similarly with 12 glycerol slides. The experiment also ran for 30 seconds, with a wind speed of 8, 10, and 11ms^{-1} and a relative humidity of 20, 35, and 50%, and was replicated 3 times. The DustTrak monitors were not used in the reference experiment as there was no need to measure dust emission from the sand.

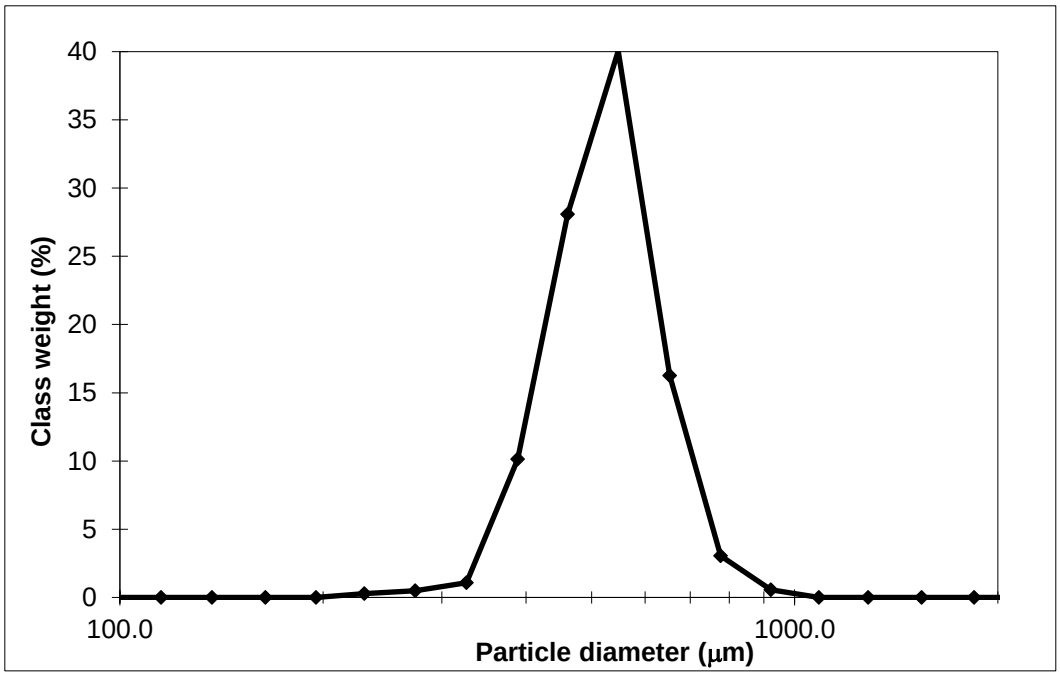

Figure 2.10. Sieve analysis of the grain size distribution of the control sand showing a mean diameter of 536 µm.

A second reference experiment was conducted to address the second research goal of characterizing the dispersion within the dust cloud as it moved downwind. The same methodology described in section 2.4.1 for the 500 µm aggregate dispersion regime experiments was followed. However, instead of the aggregates, 1 g of the pulverized silt (63 µm) particles was dropped down the tube into the wind tunnel. In this set of experiments, the properties of the dust plume that developed were independent of particle saltation and fracture. Essentially, changes in the dust concentration (i.e., downwind dilution, as typified in plume dispersion models) were solely due to dispersion from the point of entry at the upwind delivery tube.

2.4.3 Control Volume Method and Indices

In order to provide meaningful insight regarding the dispersion of dust through the wind field, the vertically integrated mass transport rate (M, mg s^{-1}) was calculated using all PM_{10} concentration data measured for a given DustTrak station. Each station defined the boundary of a control volume for which the difference between the mass moving in and out over a given period of time determined whether net dust deposition, production, or resuspension was occurring.

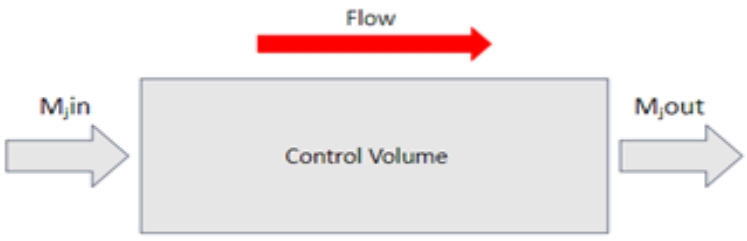

Figure 2.11. Diagram of control volume method, where $M_j$in is the incoming integrated mass transport rate in a given control volume (j), and $M_j$out is the outgoing integrated mass transport rate.

Initially, the mass transport rate (mg s^{-1}) was obtained for each respective elevation band using the following equation (E3),

$$m_i = C_i \cdot \Delta z \cdot u_i \cdot w \qquad (E3)$$

where C_i is the PM_{10} concentration (mg m^{-3}) at a given elevation i, w is the tunnel width, Δz is the difference in elevation (m), and u_i is the particle velocity at the given elevation (m s^{-1}). The vertically integrated mass transport rate (M) then was calculated from E4, for each measurement station.

$$M = \sum_{i=1}^{7} m_i \qquad (E4)$$

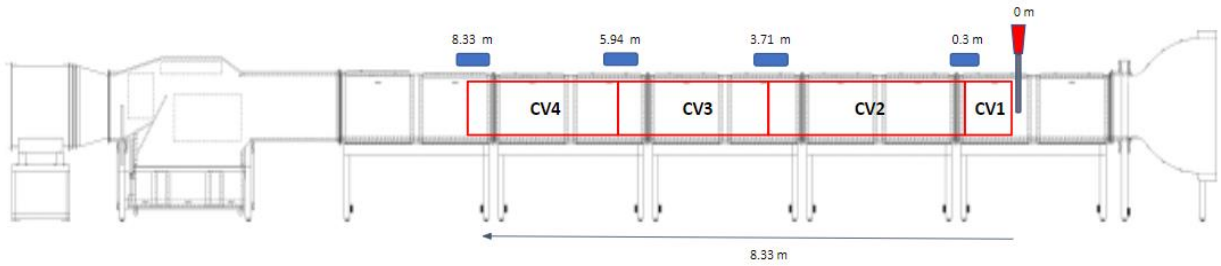

Figure 2.12. Diagram showing each control volume within the working section of the TEWT, bounded by the four DustTrak profiling stations.

Also, the mass flux rate was obtained for each control volume (CV_j) using,

$$Q_j = (M_j out - M_j in) \div A_{sj} \qquad (E5)$$

where j is the control volume number from 1-4 (Fig. 3.12), and $A_{sj} = w \cdot L$; (i.e., the basal area of control volume j). If it is found that $M_j$out is less than $M_j$in, then the flux is negative and net particle settling is occurring, whereas if $M_j$out is greater than $M_j$in, the flux is

positive, meaning PM is being produced within the control volume, either through abrasion or resuspension.

Lastly, in order to assess directly how effective saltation is in producing dust relative to an unrestricted supply of silt with equivalent mass, an efficiency index (E) or mass ratio was calculated by dividing the vertically integrated mass transport rate for the 500 μm (M_{500}) particles by that for the pulverized particles with diameter < 63 μm (M_{63}).

Chapter Three: Results

3.1 Particle Characteristics: Mineralogy, Form, and Structure

Using XRD, the Owens Lake sediments were determined to be primarily composed of quartz, albite and calcite, with minor amounts of halite and hydrophilite. With regard to their form and potential for dust production, Figs 3.1 and 3.2 a-h provide several examples of SEM images captured from small amounts of the 500 µm Owens Lake sediment. These were collected independently, representing particles collected from either the aggregate source material (SM) produced in the concrete mixer or the saltation trap (ST) following their transport down the wind tunnel. Within the SM there appear to be both aggregates (Fig. 3.1; particle 2) and dust coated sand particles (Fig. 3.1; particle 1). The surface of particle 1 (P1) is smooth with a coat of small dust sized chips (Figs. 3.1 a-d). Particle 2 (P2) has a higher degree of angularity than P1 with notable surface asperities covered in large flakes (Figs. 3.1 e-h). Particles like P2 could be susceptible to spalling due to the high likelihood of fracture intersection. After saltating through the tunnel, the aggregates shown in Fig. 3.2 appear similar in their gross form and size to those in Fig. 3.1. However, fine scale striations are apparent on the surfaces of both P1 and P2 shown in Fig. 3.2, which might be attributed to abrasion arising from rolling or sliding.

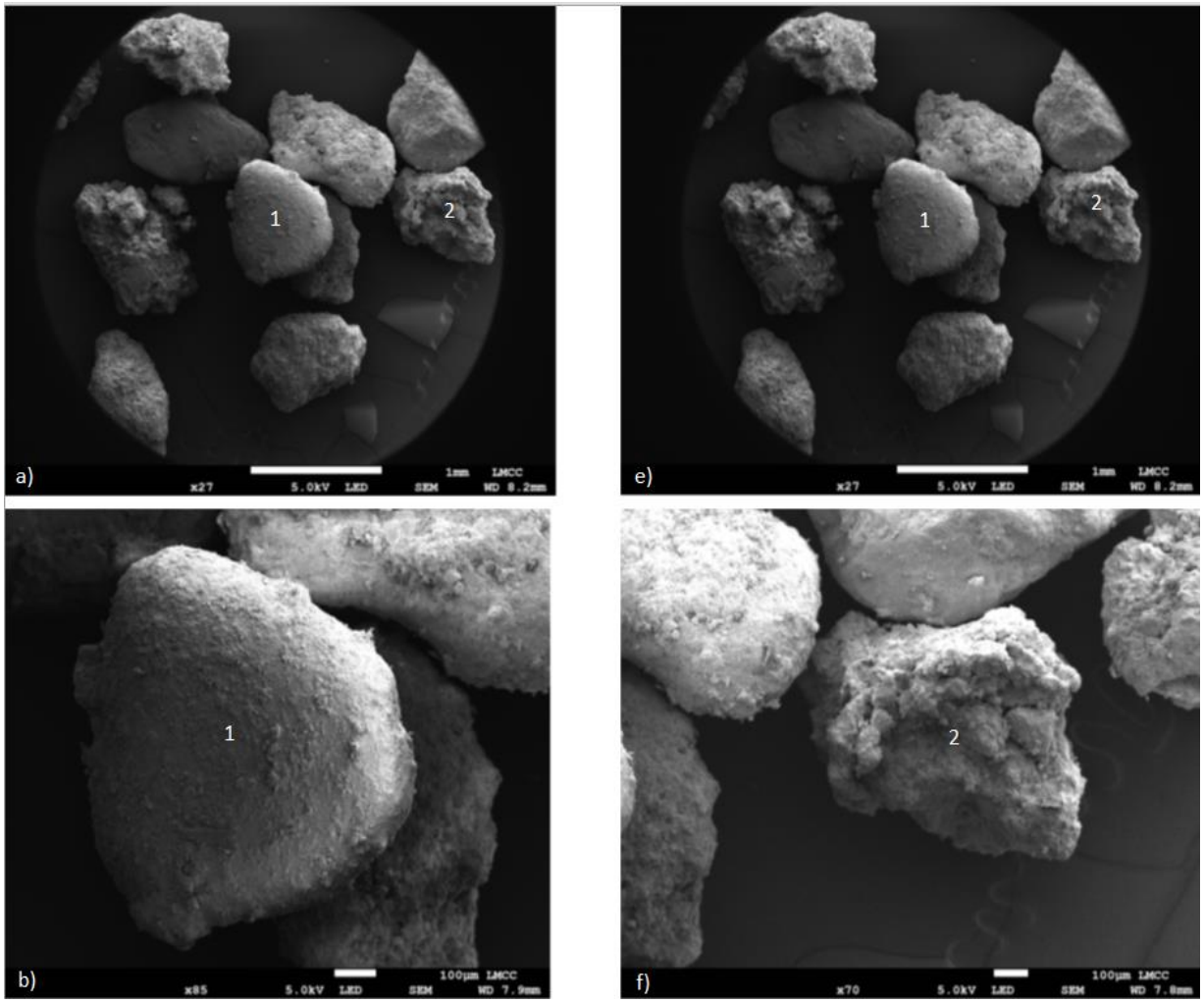
a)
1
2
x27 5.0kV LED SEM 1mm LMCC WD 8.2mm
e)
1
2
x27 5.0kV LED SEM 1mm LMCC WD 8.2mm
b)
1
x85 5.0kV LED SEM 100µm LMCC WD 7.9mm
f)
2
x70 5.0kV LED SEM 100µm LMCC WD 7.8mm

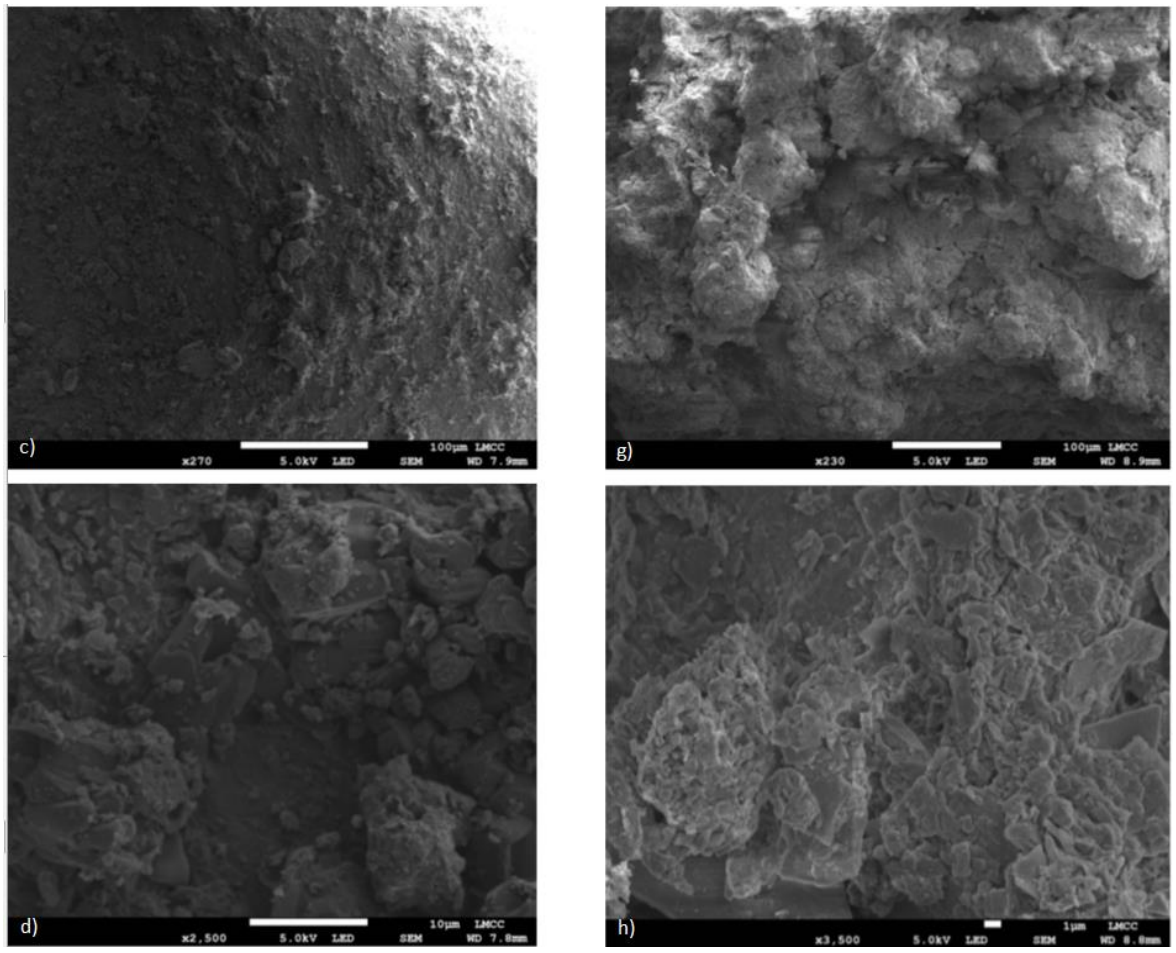

Figure 3.1. SEM images of two 500 µm SM particles shown with increasing magnification. Images a) to d) are P1 with increasing magnification from a) 27x, b) 85x, c) 270x though d) 2500x. Images e) to h) are P2 with increasing magnification from a) 27x, b) 70x, c) 230x, through d) 3500x. SEM photo credit: Material Science Labs, Loughborough University.

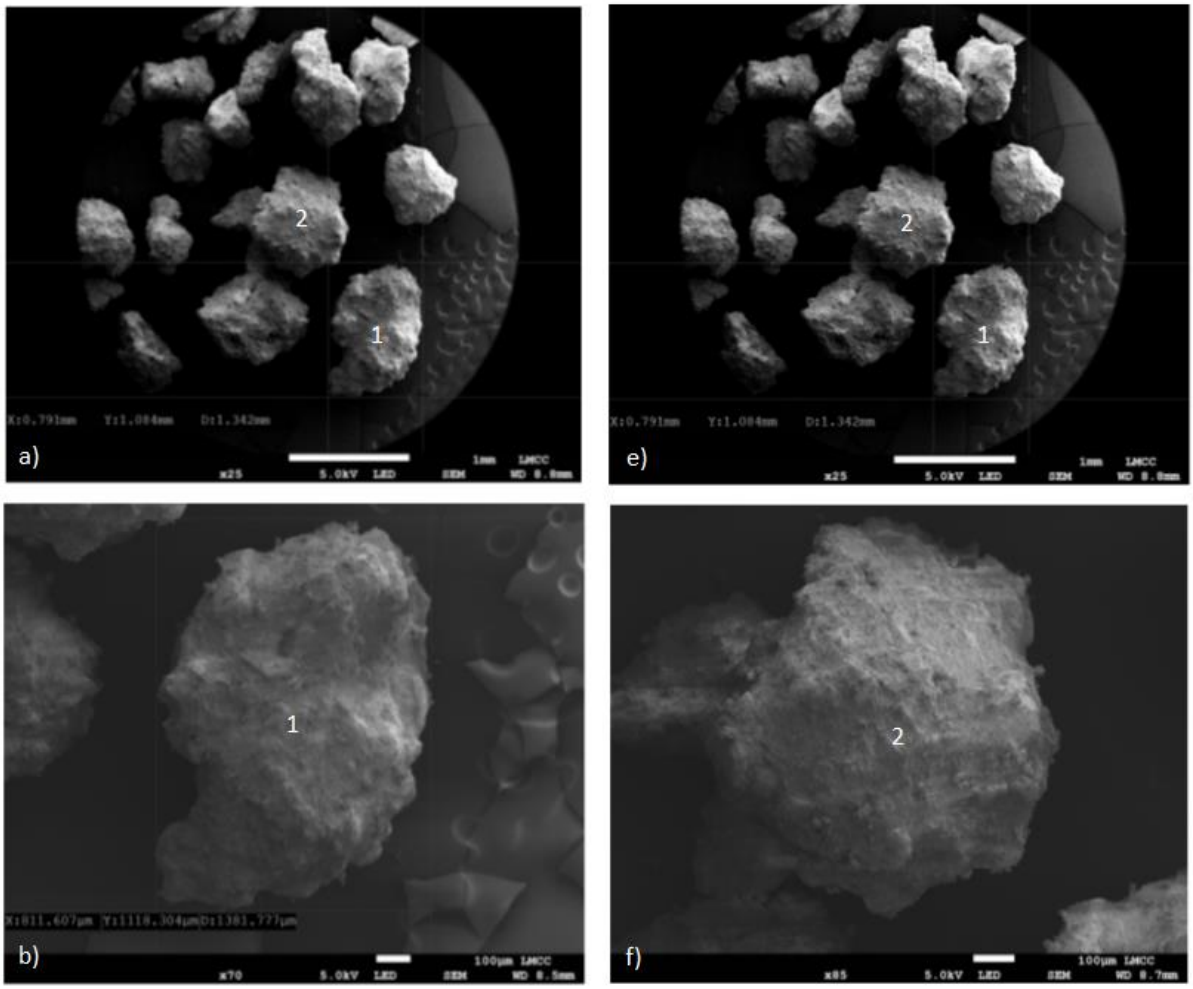
2
1
a)
2
1
e)
1
b)
2
f)

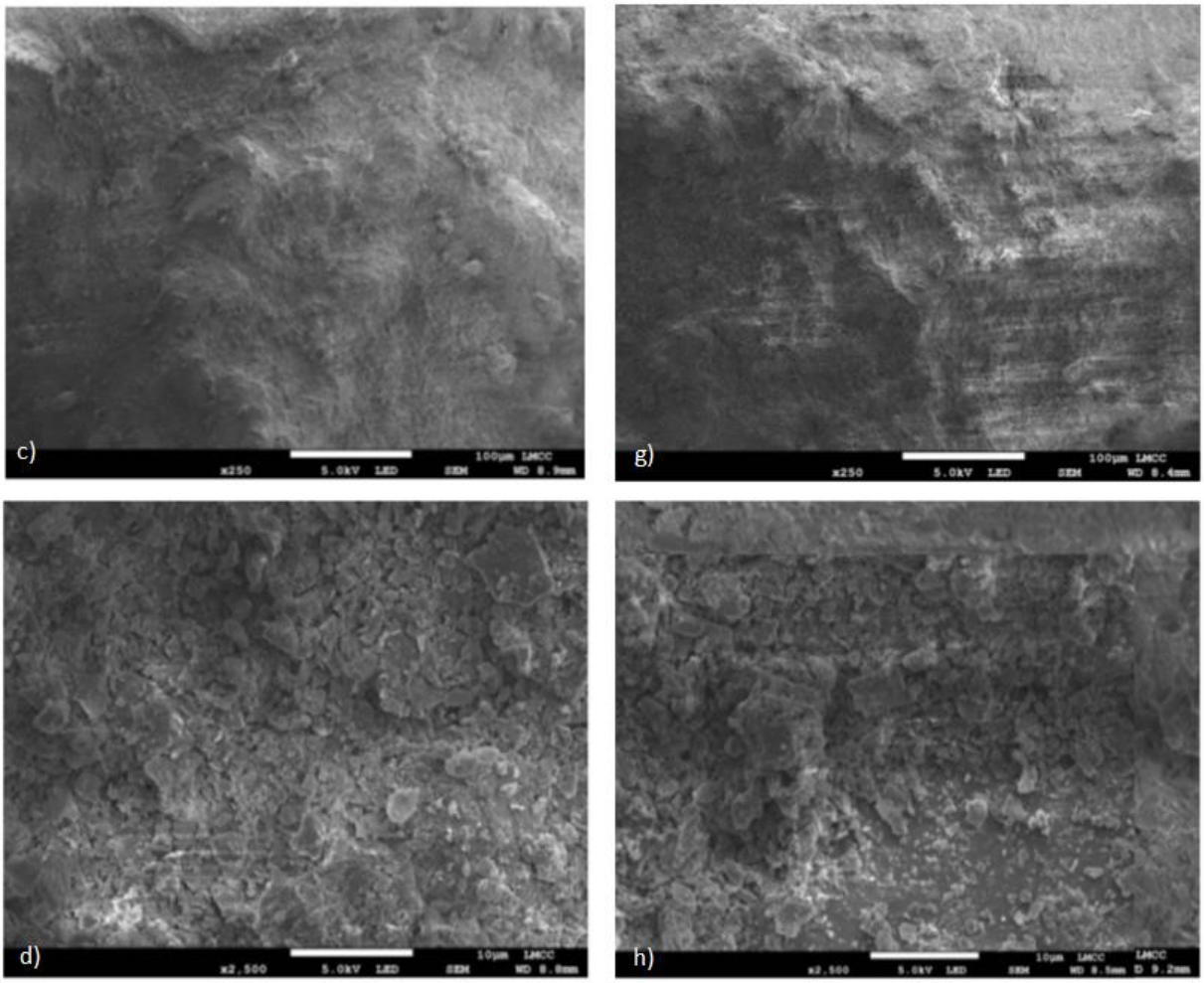

Figure 3.2. SEM images of two ST aggregates, initially 500 µm, after saltating 8 m over the rough floor. Images a) to d) are P1 and images e) to h) are P2 with increasing magnification from 25x, 70x, 250x, and 2500x. SEM photo credit: Material Science Labs, Loughborough University.

3.2 Airflow and Particle Speed Characteristics in the Wind Tunnel

The first purpose of this section is to describe the airflow structure within the working section of the TEWT, as this will affect the dispersion of dust and the formation of a plume originating at the delivery tube. The second purpose of this section is to evaluate the speed of the particles as they moved through the working section of the wind tunnel.

The isovel plots for the vertical component (v) of the flow velocity appear to vary with the fetch and are very different between 6 and 8 m downwind (Figs. 3.3 a and b). At 6 m the values for v are all negative, which indicates downwelling flow. At 8 m, the flow is downwelling from the top two corners of the wind tunnel towards the bed, then moving upwards (upwelling) in the middle of the tunnel. This shows instability within the vertical flow (i.e., secondary flow), which can arise within any confined flow. This is an artifact of the wind tunnel structure and is expected in any straight-line facility.

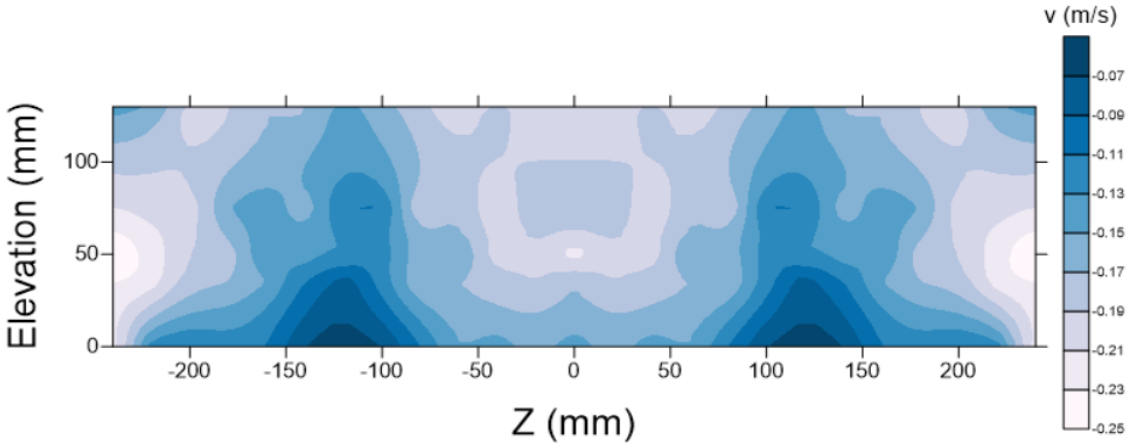

a)

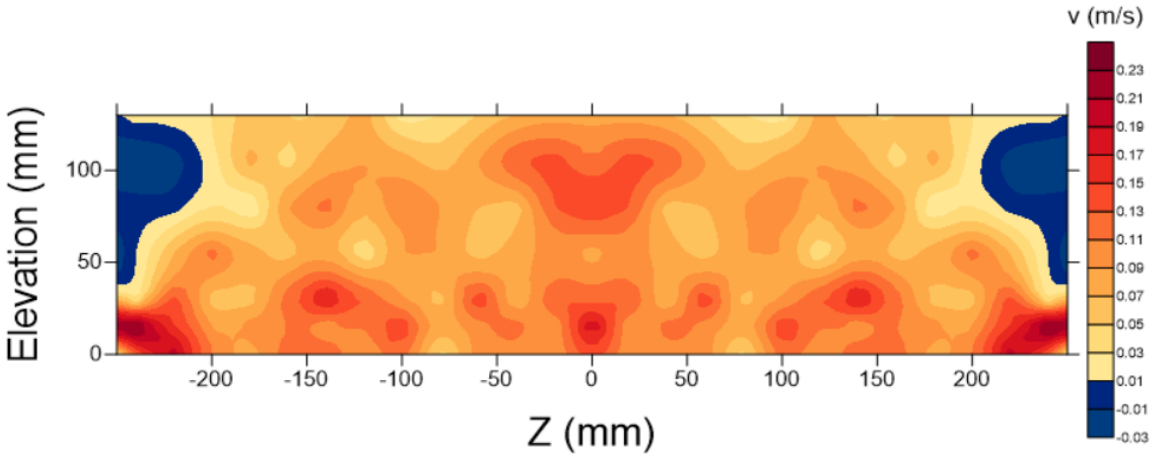

b)

Figure 3.3 a-b. Isovel plot of the vertical velocity along a grid plane oriented normal to the mean flow at a) 6 m and b) 8 m downwind of the sediment delivery tube.

During wind erosion events, abrasion of soil aggregates is often a source of erodible-sized particles; however, little is known about the physics of particle abrasion. As such, these velocities are appropriate for calculating the dust flux, but not that of the coarse particles. It is further assumed that if the dust is carried in suspension, the particles move at the speed of the airflow, or very close to it, so that the velocity profiles plotted in Figs. 3.4 a) to h) approximate those of the airflow. Similar to the trends shown in the isovel plots in Fig. 3.3, for which the flow was seeded with glycerine fog particles, the profile of the vertical component show dust is subject to downwelling at ≈ 4 and 6 m and upwelling at 8 m (Fig. 3.5). In Fig. 3.5 b, c, f, and g, the velocity measurements are mostly negative, indicating downwelling, whereas in Fig. 3.5 d and h, the velocity values are mostly positive, indicating upwelling.

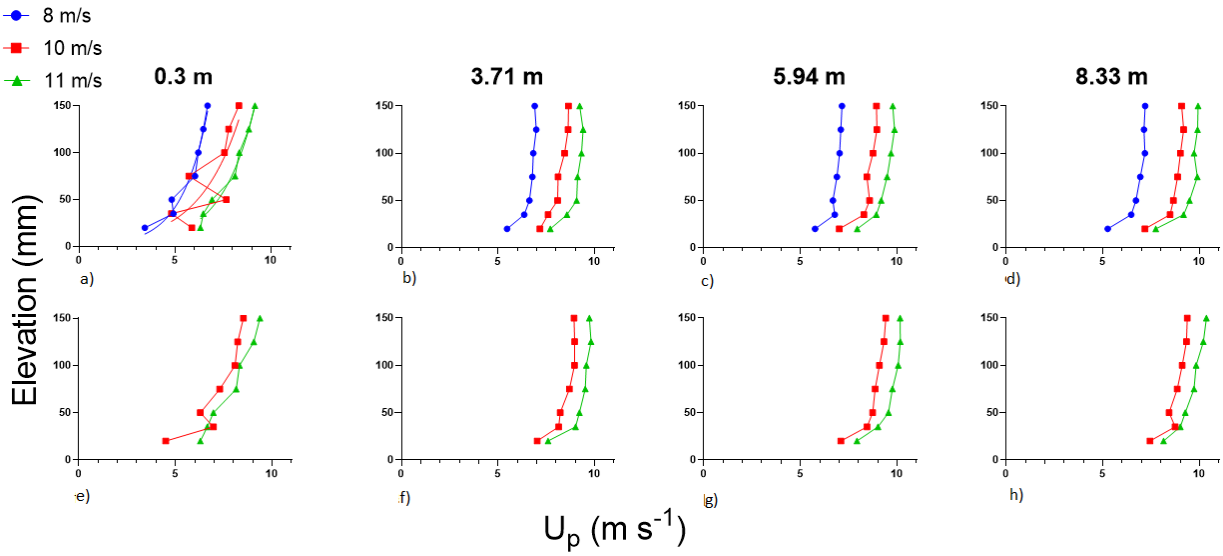

Figure 3.4 a-h. Horizontal component of the particle velocity (u_p) in vertical profile. Graphs (a-d) represent particle velocities sampled over smooth floorboards, as compared to rough floorboards (e-h).

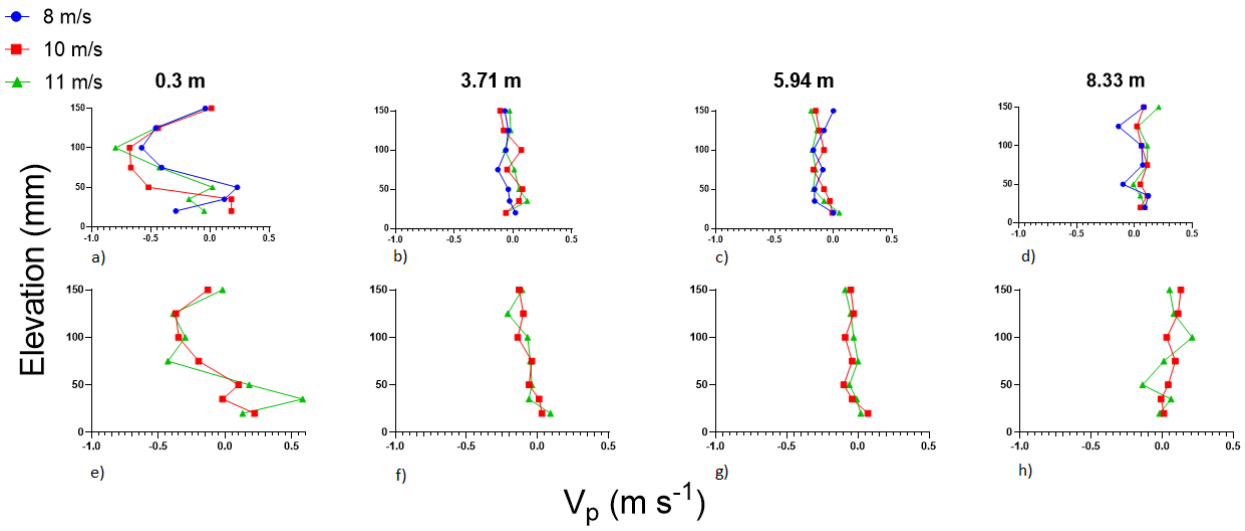

Figure 3.5 a-h. Vertical component of the particle velocity (v_p) in a vertical profile. Graphs (a-d) represent particle velocities sampled over smooth floorboards, as compared to rough floorboards (e-h).

The shear velocity values calculated from vertical profiles of the horizontal particle speed (Fig. 3.4) using E1 are presented in Table 3.1. As expected, the u_* values increase both with an increase in wind speed, and generally, distance downwind. There is also an increase in the u_* values with an increase in roughness of the bed surface. The values are not listed for 0.3 m since the particles had not yet come into equilibrium with the boundary-layer flow development after being dropped into the wind tunnel. In regard to the aerodynamic roughness length (z_o) and the degree of correlation (R^2), there are no clear trends.

Table 3.1. Summary of the u_*, z_o, and R^2 values for Fig. 3.5 a-h, with S representing smooth floor and R representing rough floor.

u_* (m/s) | z_o (m) | R^2	8 ms^{-1}	10 ms^{-1}	11 ms^{-1}
0.3 m S	–	–	–
3.71 m S	0.29 | $1e^{-5}$ | 0.87	0.31 | $4e^{-6}$ | 0.96	0.34 | $3e^{-6}$ | 0.78
5.94 m S	0.27 | $1e^{-6}$ | 0.92	0.37 | $2e^{-6}$ | 0.89	0.38 | $5e^{-6}$ | 0.93
8.33 m S	0.38 | $5e^{-4}$ | 0.89	0.39 | $1e^{-6}$ | 0.89	0.44 | $2e^{-6}$ | 0.81
0.3 m R	–	–	–
3.71 m R	–	0.39 | $3e^{-6}$ | 0.90	0.43 | $2e^{-6}$ | 0.90
5.94 m R	–	0.43 | $8e^{-6}$ | 0.98	0.45 | $1e^{-6}$ | 0.94
8.33 m R	–	0.38 | $4e^{-7}$ | 0.94	0.42 | $2e^{-7}$ | 0.98

3.3 Analysis of Particle Size Distribution on Glass Slides

In Figs. 3.6 a) and b) highly visible aggregates, with silt and sand grains cemented to their surfaces, appear on the first slide nearest to the drop tube. Moving further downwind (Figs. 3.6 b-c and e-f), the images show silt sized particles that have disaggregated in experiments with both the smooth and rough floorboards. Each microscopy image represents a fraction of the total area of the glycerol slide (≈ 0.1 cm^2) and was selected as a representative sample of

the total slide. Although the whole sampling area (1 cm^2) was not captured, three replicate images were taken of different sampling areas within each slide in an attempt to reduce bias. Each image was captured under the same lighting and magnification conditions. The number of grains examined and measured for each image varied significantly. As detailed in section 2.4.1, the customized MATLAB program used these images to quantify the particle count in each image, but also outputted the black to white ratio, particle area and perimeter, from which the particle diameter of the grains in each image was calculated using these four variables (E6).

$$D = \sqrt{\frac{a}{\pi}} \cdot 2 \qquad (E6)$$

Where a is area, calculated by the black to white percentage divided by the particle count of the image. Black and white images of the control sand and aggregate microscopy can be found in Appendix 1.4 and 1.5.

Figs. 3.7 a) and b) report the particle diameters provided by the MATLAB program. Each point symbol represents the average particle diameter over the three replicate images taken for each slide. These results confirm the apparent breaking apart or disintegration of the particle aggregates downwind, as there is a steep decrease in the particle diameter with distance, until it stabilizes around 200 μm. The purpose of the reference experiment was to evaluate the natural fining of normally distributed sand particles downwind. Although no downwind trend is apparent for the mean diameter, the sorting does improve over distance as shown by the decreasing standard deviation (error bars) in Fig. 3.7 a. When comparing the aggregate data to the reference (sand) data, the decrease in aggregate particle diameter (Figs. 3.7 a and b) well exceeds that of the control sand, the latter remaining fairly consistent in diameter with distance. This would indeed suggest that aggregate communition occurred during transport.

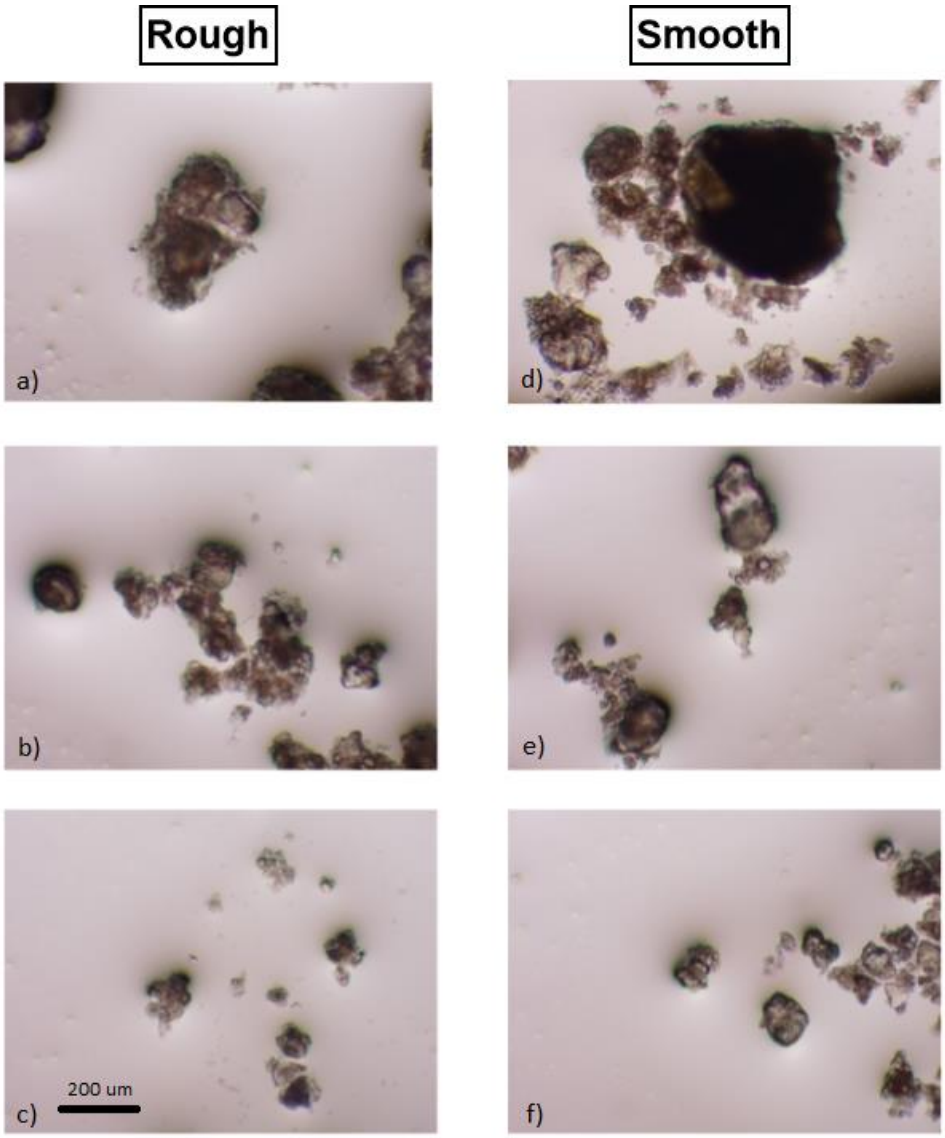

Figure 3.6 a-f. Sample microscopy images of glass slides for image replicate 1 at 11 ms^{-1} and 20% RH. Figures a) to c) refer to runs with rough floorboards at slides 0.3, 3.7, and 8.33 m downwind. Figures d) to f) refer to runs with smooth floorboards, also at slides 0.3, 3.7, and 8.33 m downwind, respectively.

a)

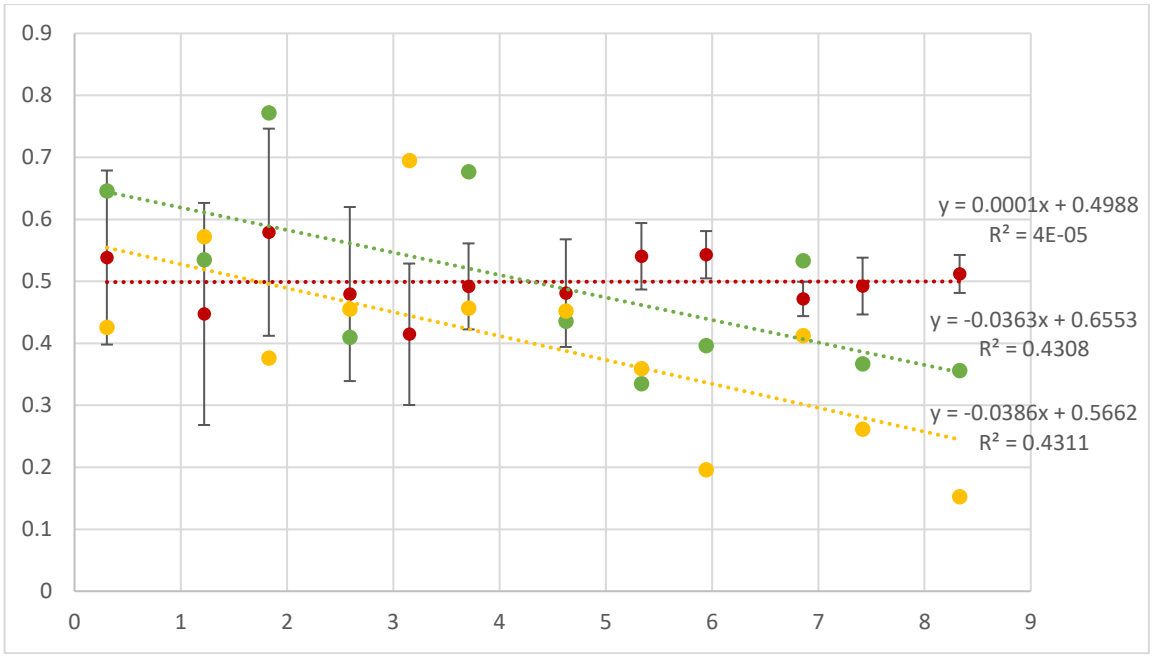

b)

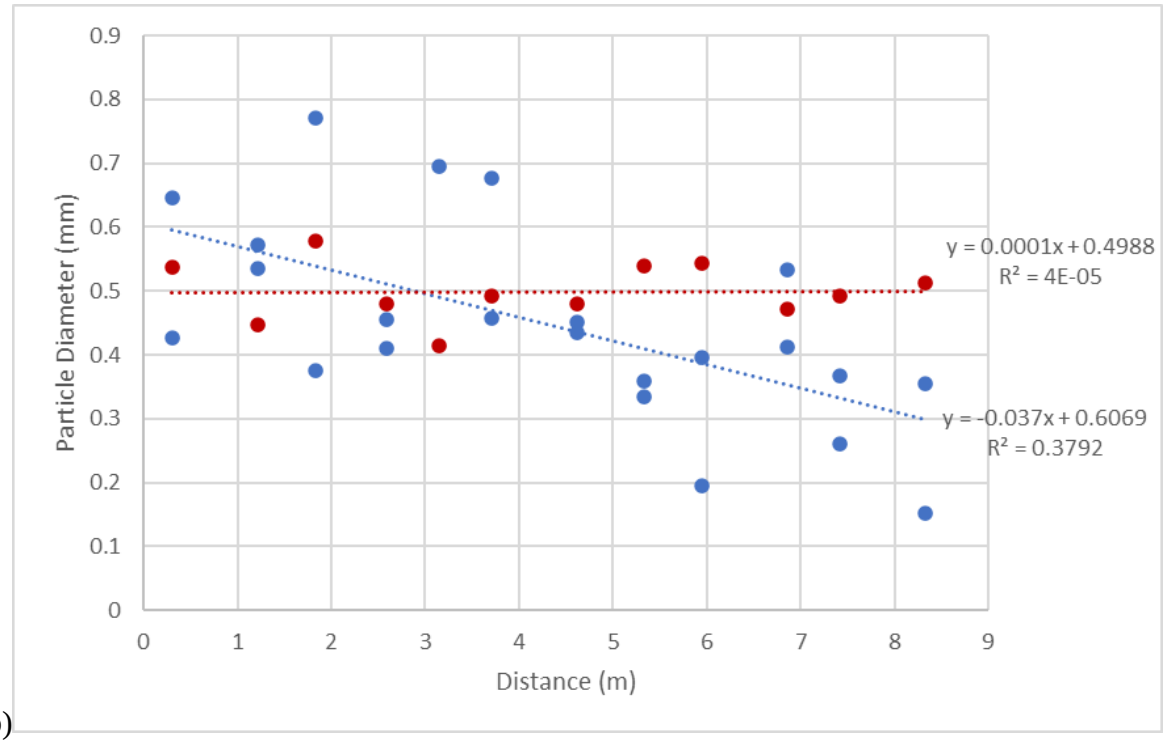

Figure 3.7 a-b. Change in mean diameter of sand (red symbols) and particle aggregates with distance of transport downwind. Figure a) refers to particle aggregates over the rough floorboard fetch (yellow symbols) and smooth floorboard fetch (green symbols). Figure b) is the result of combining the smooth and rough floor data (blue symbols).

The slope and R^2 values for the relation are similar between the rough and smooth surfaces. In essence, the surface texture did not seem to influence the rate of aggregate breakdown with distance. The intercept represents the particle size after being dropped into the tunnel. The particle size is generally smaller after the first impact for the rough surface than for the smooth. However, when the data are pooled regardless of roughness, the regression equation is roughly the same but the R^2 value decreases. On the other hand, the slope of the control sand equation is constant, with little change over distance, and the intercept is around the mean particle diameter for the control sand.

3.4 Reference Experiments with Pulverized Silt

The reference experiments, in which pulverized silt was introduced in the airflow, support the results for the particle aggregate experiments as they provide insight into how dust was dispersed through the wind field in the absence of saltation. Several examples of the decay in the PM_{10} concentration measured with increasing distance from the tunnel floor for selected experiments with varied relative humidity and a constant freestream velocity of 11 ms^{-1} are displayed in Fig. 3.8. The dust concentration in the absence of saltation was not affected by humidity but did increase with increasing roughness of the bed surface. Lastly, Fig. 3.8 demonstrates that there is little inter-run variability in terms of the plume system as the values are fairly consistent between runs, with the exception of the rough floorboard experiments at 8.33 m downwind.

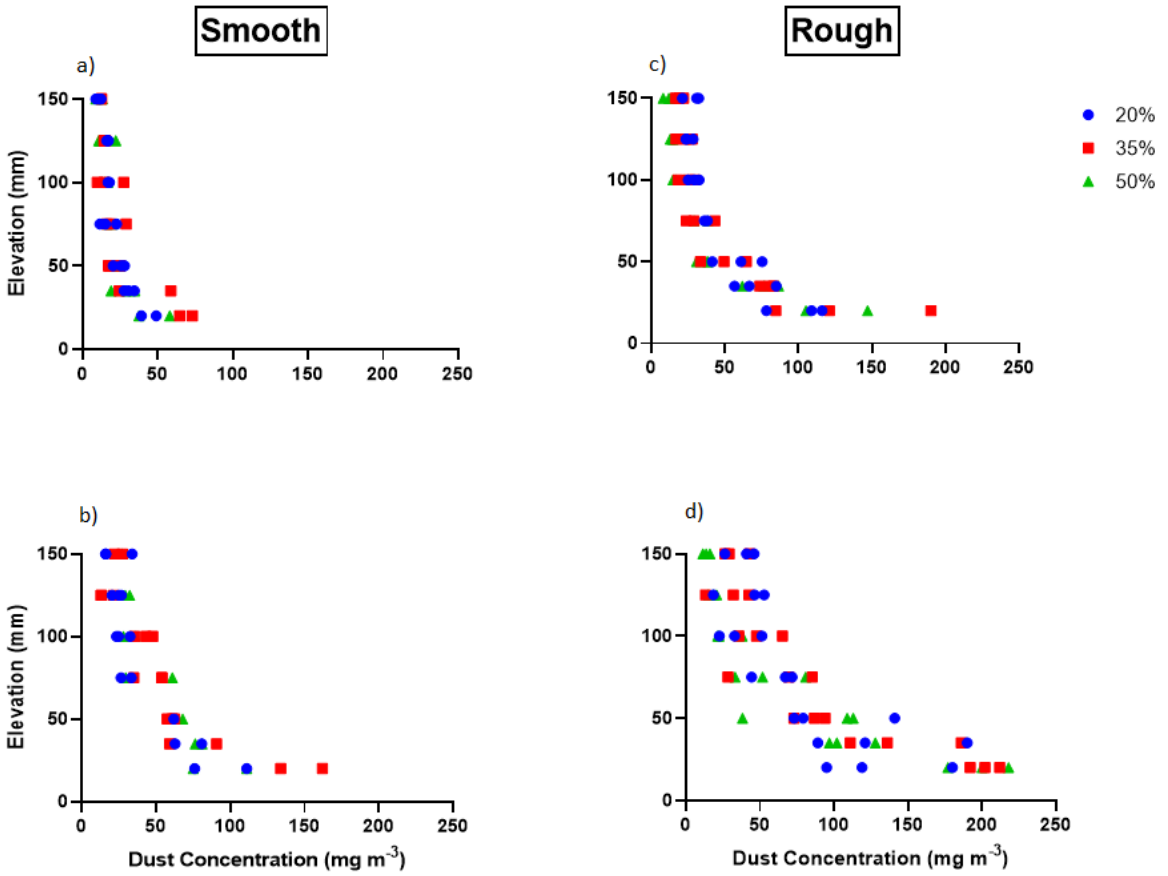

Figure 3.8 a-d. Sample plot of the variation in PM_{10} concentration (mg m^{-3}) with elevation (m) for pulverized silt particles under 63 µm diameter. Plots a) and b) refer to runs with smooth floorboards at downwind distances of 3.71 m and 8.33 m, respectively. Plots c) and d) refer to runs with the rough floorboards, also at downwind distances of 3.71 m and 8.33 m, respectively. Freestream velocity for all experiments was 11 ms^{-1}.

Interestingly, the vertically integrated mass transport rate (M), shown in Fig. 3.9, consistently decreases between the DustTraks located at 0.3 m and 3.71 m, shows little change between 3.71 and 6 m, and increases slightly between 6 m and 8 m. Variation in roughness, wind speed and humidity appear to have little effect on either this general trend or the magnitude of the mass transport rate.

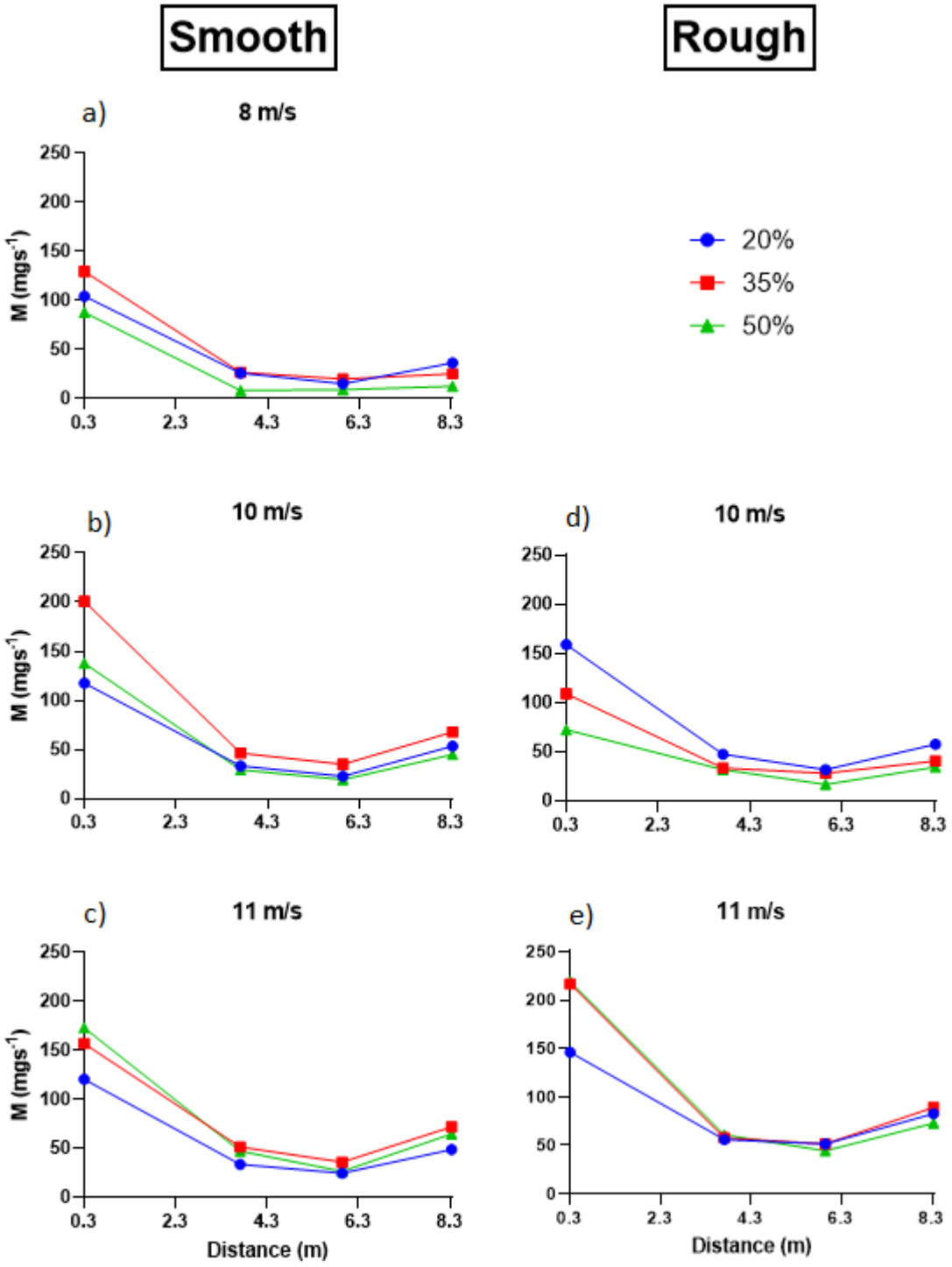

Figure 3.9 a-e. Vertically integrated mass transport rate in mg s^{-1} with distance (m) for pulverized silt particles under 63 μm diameter. Plots a), b) and c) refer to runs with smooth floorboards at wind speeds of 8 ms^{-1}, 10 ms^{-1} and 11 ms^{-1}, respectively. Plots d) and e) refer to runs with the rough floorboards, also at wind speeds of 10 ms^{-1} and 11 ms^{-1}, respectively.

With reference to the experiments carried out for this study, Fig 3.10 shows a very large positive flux (bars - solid fill) within CV_1 immediately downwind of the sample delivery tube. This is expected since the dust input upwind of the tube is null. Within control volumes 2 and 3, the flux values are negative (bars - textured fill), meaning that some degree of settling is occurring since $M_j$out is less than $M_j$in. Within the control volume furthest downwind (CV_4), however, the flux is positive once again, meaning some degree of resuspension, likely due to upwelling, is occurring since $M_j$out is greater than $M_j$in. This general pattern is independent of all experimental conditions or varied wind speed, humidity, aerodynamic roughness.

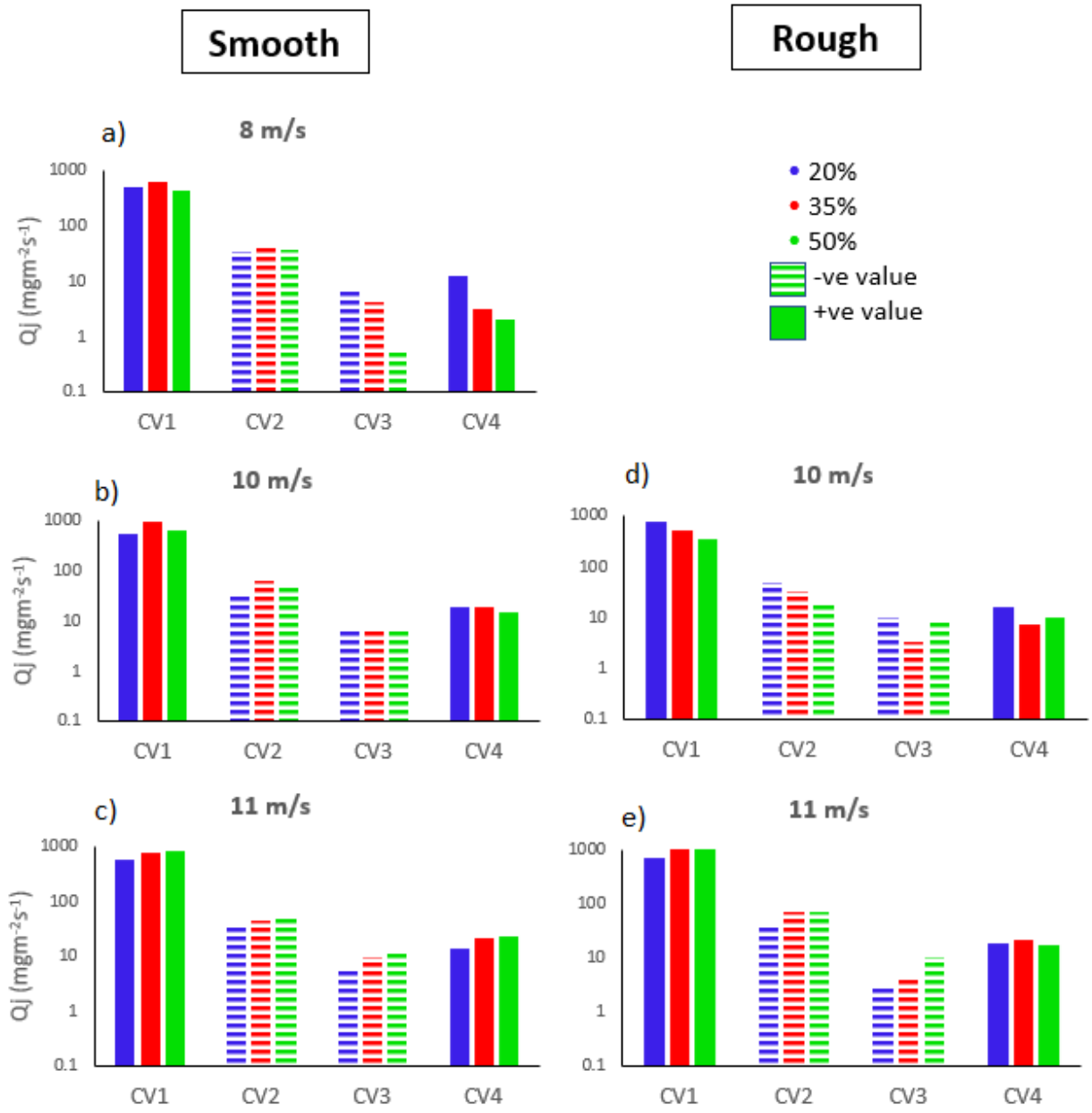

Figure 3.10 a-e. Mass flux rate for pulverized silt particles under 63 μm diameter. Plots a), b) and c) refer to runs with smooth floorboards at wind speeds of 8 ms^{-1}, 10 ms^{-1} and 11 ms^{-1}, respectively. Plots d) and e) refer to runs with the rough floorboards, also at wind speeds of 10 ms^{-1} and 11 ms^{-1}, respectively.

3.5 Saltation Experiments

One of the main goals of this study was to assess dust generation during the saltation of sediments collected from the Owens Lake playa, as well as the associated influence of varied surface roughness, wind speed and relative humidity. The PM_{10} concentration in a vertical profile and its variation along the working section of the wind tunnel is illustrated in a small selection of sample plots in Fig. 3.11. Similar to the profiles for the pulverized silt shown in Figs. 3.8 a-d, the vertical profiles show a decay in PM_{10} concentration with height and an increase with greater bed roughness and fetch (Fig 3.11). However, the concentration of PM_{10} sampled is substantially lower for the 500 μm aggregates. Near the bed surface, the concentration does not exceed 40 $mg \cdot m^{-3}$ for the experiments with saltation but was generally twice as large (or more) for the pulverized silt in the reference experiments. In the case of the rough floorboards, humidity has a clear influence on dust concentration in the presence of saltation, but this relation does not hold true for the smooth bed surface.

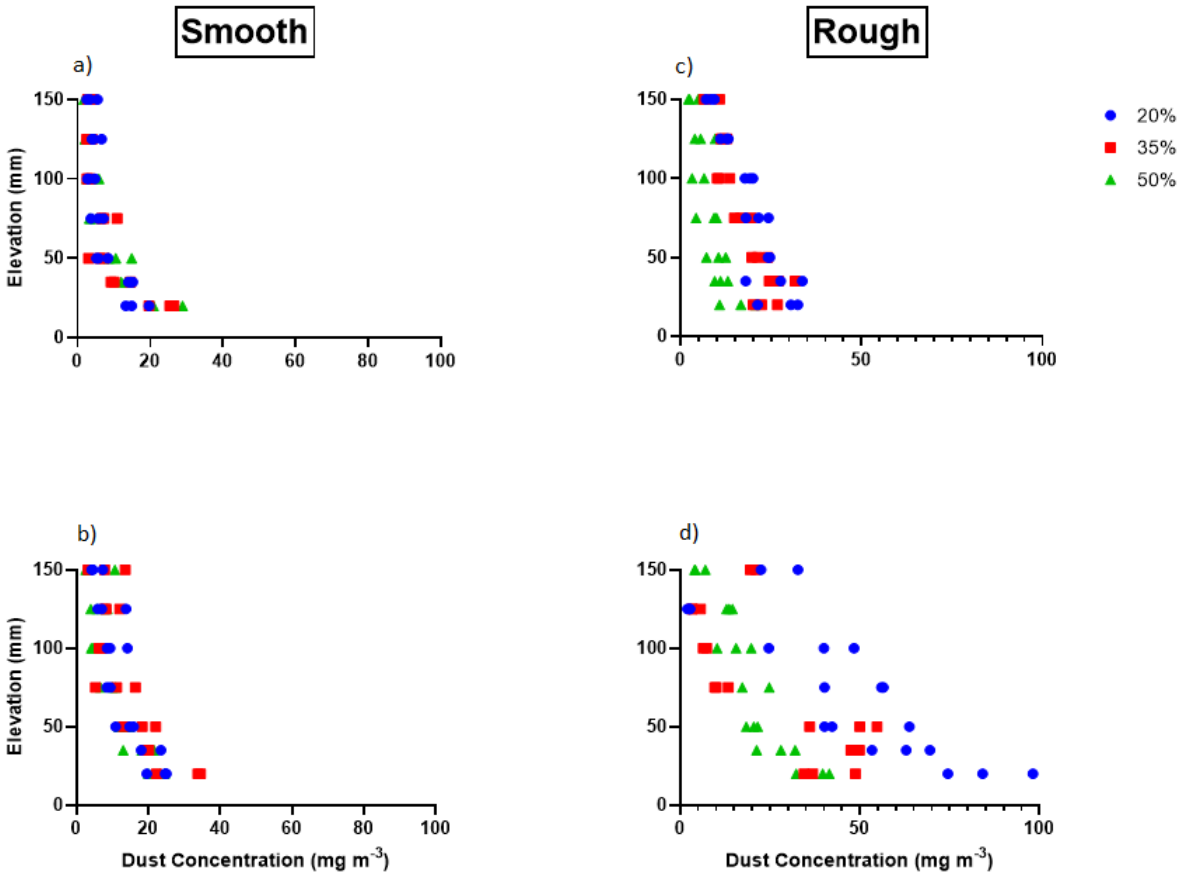

Figure 3.11. Sample plot of the variation in PM_{10} concentration (mg m^{-3}) with elevation (m) for particles with a diameter of 500 µm. Plots a) and b) refer to runs with smooth floorboards at downwind distances of 3.71 m and 8.33 m, respectively. Plots c) and d) refer to runs with the rough floorboards, also at downwind distances of 3.71 m and 8.33 m, respectively. Freestream velocity for all experiments was 11 ms^{-1}.

As described in section 2.4.3, M (Fig. 3.12) and Q_j (Fig. 3.13) were calculated to assess PM_{10} production from saltation of the 500 µm particles. The mass transport rates are much lower than for the pulverized silt, while the change with distance downwind is more subdued, though somewhat in a similar pattern. However, there is not an immediate and very large input of dust from the drop tube as in the case of the silt. Overall, there is still a small upturn

in the relation around 8 m downwind with the pulverized silt, with no clear role for relative humidity.

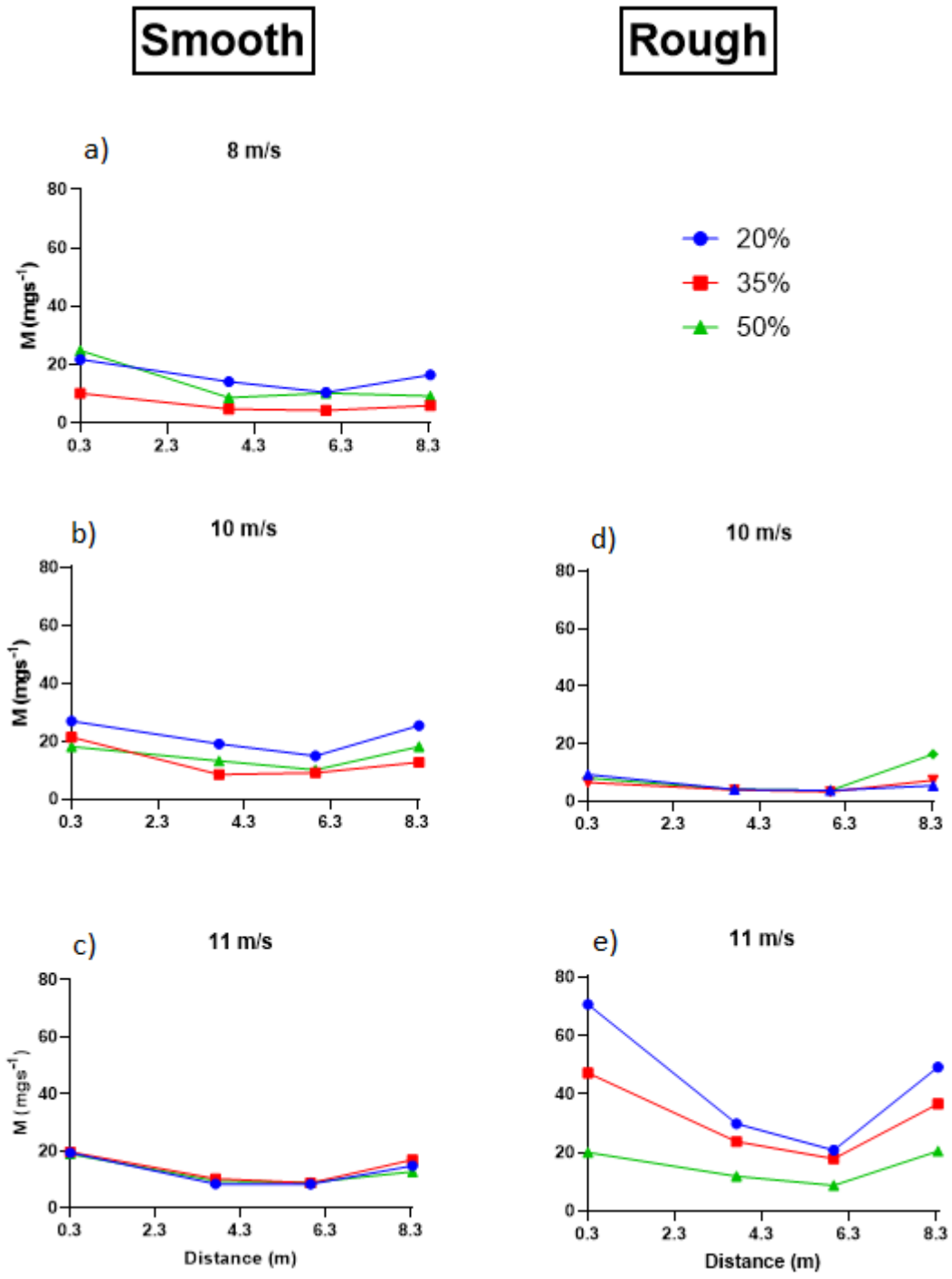

Figure 3.12 a-e. Vertically integrated mass transport rate in mg s^{-1} with distance (m) for particles with a diameter of 500 µm. Plots a), b) and c) refer to runs with smooth floorboards

at wind speeds of 8 ms^{-1}, 10 ms^{-1} and 11 ms^{-1}, respectively. Plots d) and e) refer to runs with the rough floorboards, also at wind speeds of 10 ms^{-1} and 11 ms^{-1}, respectively.

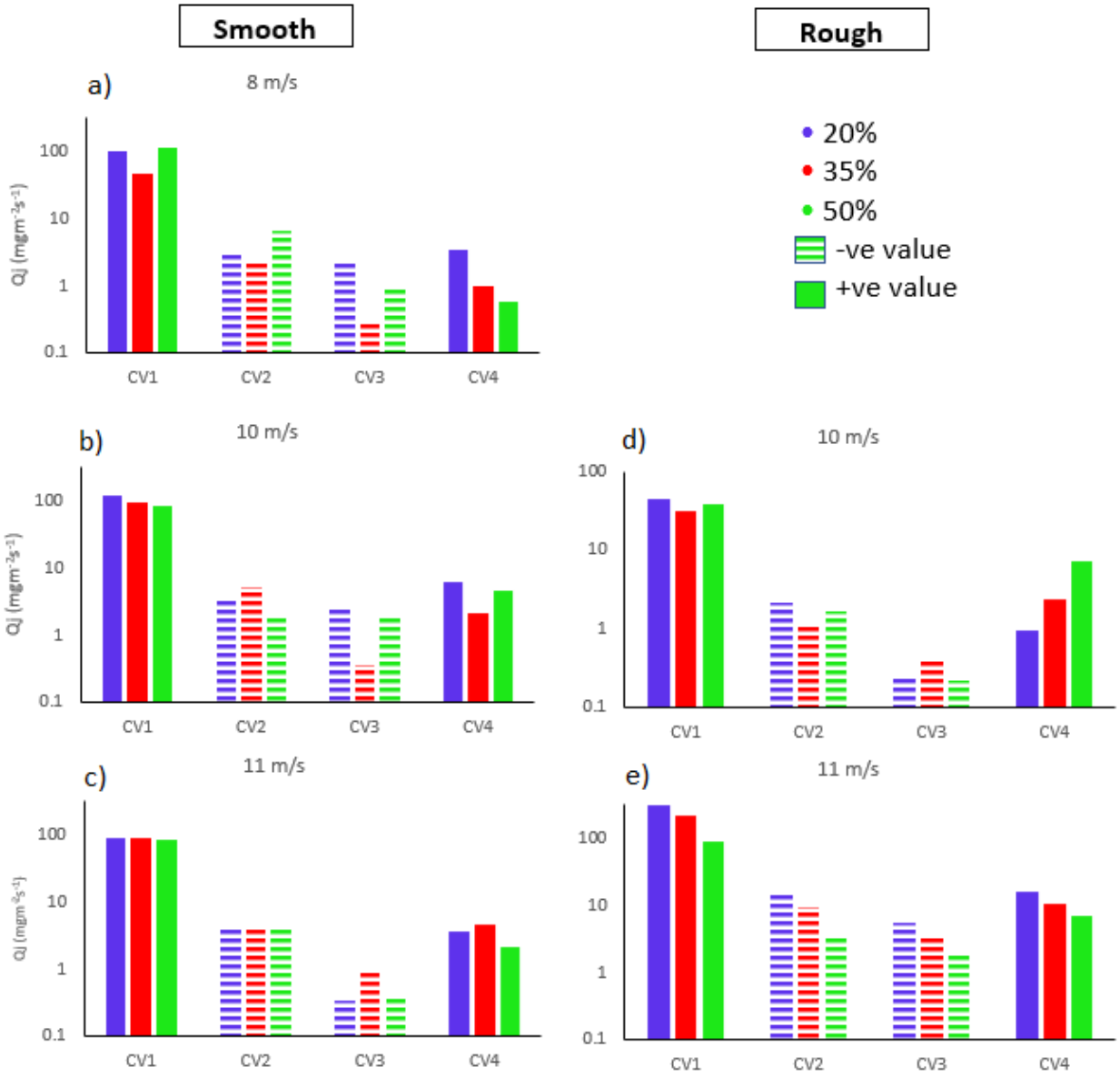

Figure 3.13. Mass flux rate for particles with a diameter of 500 µm. Plots a), b) and c) refer to runs with smooth floorboards at wind speeds of 8 ms^{-1}, 10 ms^{-1} and 11 ms^{-1}, respectively. Plots d) and e) refer to runs with the rough floorboards, also at wind speeds of 10 ms^{-1} and 11 ms^{-1}, respectively.

As compared to Fig. 3.10, the PM_{10} fluxes for the saltating particles shown in Fig. 3.13 are generally an order of magnitude lower, yet still show similar trends with distance downwind. Large positive values are associated with the control volume nearest the sediment delivery tube, and negative values with CV_2 and CV_3. The flux is once again positive for CV_4. Changing wind speed, humidity, and roughness do not appear to consistently alter the dust flux.

Calculation of the mass ratio from the reference and aggregate experiments, detailed in section 2.4.3, removes the effect of the flow structure within the tunnel (Fig. 3.3) that is shown to strongly affect dust dispersion. Overall, the mass ratio is very low or less than 5%. E tends to increase with the distance of particle transport, but fetch plays a greater role for the smooth floor as compared to the rough floor. On the smooth bed, the ratio drops with an increase in the wind speed and the assumed particle trajectory length. It is also shown that E is generally highest at 20% RH (Fig. 3.14).

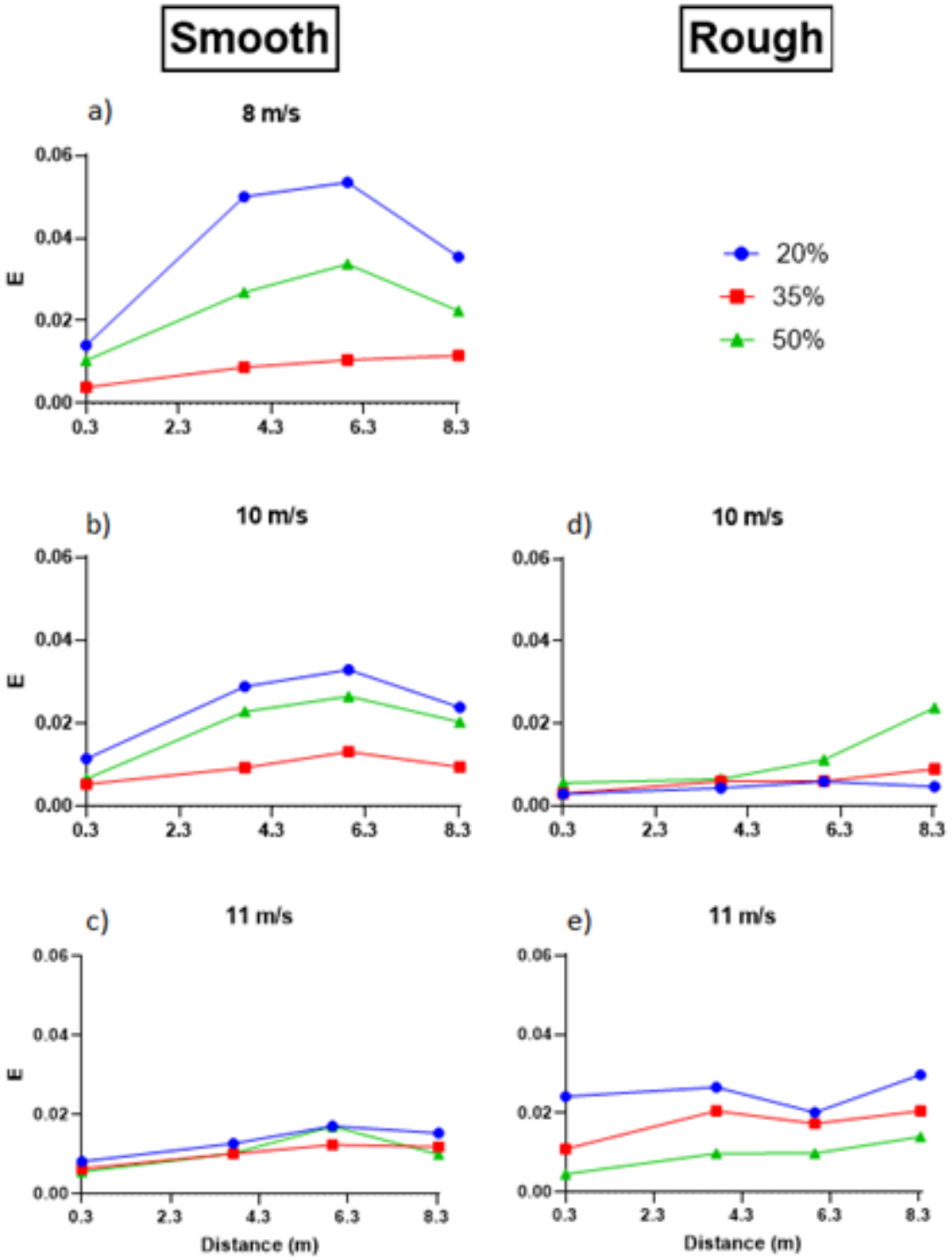

Figure 3.14 a-e. Mass ratio, as a decimal, resulting from normalizing M for 500 μm aggregates by M for 63 µm pulverized silt. Plots a), b) and c) refer to runs with smooth floorboards at wind speeds of 8 ms^{-1}, 10 ms^{-1} and 11 ms^{-1}, respectively. Plots d) and e) refer to runs with the rough floorboards, also at wind speeds of 10 ms^{-1} and 11 ms^{-1}, respectively.

Chapter Four: Discussion

4.1 Aggregate Breakdown

There is direct evidence of a size reduction independent of sorting processes that has been validated with a control. The first hypothesis listed in Ch 1, in which aggregate particle diameter would decrease linearly with increasing distance of transport, is supported by the evidence obtained. This is supported in part by the rate at which the particle size decays. The rate of decay is constant, not exponential, meaning the rate does not change with distance over the short fetch considered. The rate based on mean values is about 0.036 mm or 36 μm per meter of transport. This is equivalent to losing a silt particle from an aggregate with every meter travelled. Notably, the decrease in aggregate diameter well exceeds that measured for the natural sorting observed for the sand particles, as shown in the images in Figs. 3.7 a and b, clearly supporting the claim that aggregate size reduction is present during transport. The R^2 value for the relation is ~0.43, confirming that there is a correlation, although about 60% of the total variation in the means remains unexplained by the distance of transport. Since the data are lumped across all experiments, the noise in the relation might be explained in part by varying wind speed or humidity. It is further important to acknowledge the large variation in particle diameter observed within any given slide. Since the area assigned to catch the particles is relatively small in comparison to that of the wind tunnel floor, it limits the particles captured to a similarly small sample size. Also, some of the breakdown may have occurred within the drop tube before particles struck the tunnel floor.

A similar field wind tunnel study (also supporting H1) found a significant change in aggregate size distribution during dust emission processes (Swet and Katra, 2016). Their experiments were also conducted with a boundary layer wind tunnel with a fetch of 7 m;

however, it was operated on bare surfaces of four soils and set to two different wind speeds: 5 ms^{-1} to represent a velocity above threshold of saltators, and 9 ms^{-1} to represent aeolian erosion. Bulk concentrations of suspended particles, rather than throughout the working section fetch, were measured by a single DustTrak at intervals of 1 s. Their data show that the disaggregation of the larger aggregates (>500 µm) downwind increased the number of saltator-sized aggregates (63–250 µm), which affected the rate of the dust emission over time. This study defines 63-250 µm particles as saltators. They used a Sensit sensor that converted the impact energy of the saltating particles into number of impacts. Their findings are very similar to the results from the present study shown in Figs. 3.7 a and b, wherein the 500 µm aggregates introduced through the drop tube are reduced in size through spalling to about half their original diameter at about 8 m. However, the fetch in Swet and Katra's (2016) experiments was similar to that in this study, therefore the limitations associated with this short distance still apply.

The bed surface roughness did not appear to have a significant influence on aggregate fining over distance. This outcome refutes H2, which predicts that aggregate particle diameter decreases at a higher rate as the surface becomes rougher. Although an offset is apparent, the particle decay rates are very similar for the rough and smooth floors (Fig. 3.7 a). This would further suggest that any enhancement of the suspended dust concentration with increased bed roughness is most likely associated with greater turbulence intensity. In contrast, earlier studies (Swet and Katra, 2016; Gelbart and Katra, 2020) report that an increase in shear velocity, arising from greater surface roughness, increased dust emission. Through inference, the authors attribute this outcome to increased aggregate breakage. However, they do not report or quantify the direct effect of surface roughness on aggregate breakdown. The direct

correlation between surface roughness and aggregate breakdown has not been examined in detail, as it was in this study, thus comparison with the literature is not possible.

There are three factors to consider when particle aggregates are transported over some distance: i) particles are more likely to remain or be re-entrained in saltation as they become increasingly smaller and lighter, ii) total surface area susceptible to rupture increases, and iii) the number of tiny stress fractures on a particle surface increases with the number of impacts. As the active surface area increases due to fracturing, dust emissions are likely to increase exponentially. As shown in Figs. 3.1 a-h, the surface of the imaged particles is rough and flaky. With each impact on the bed surface during saltation, a number of surface fractures may form on these aggregates. When these fractures intersect, it is plausible that a small mass could break off. However, even after saltating over an 8 m fetch, the surface texture of the particle aggregates shown in Figs. 3.2 a-h appears similar to those in Figs. 3.1, which were not blown through the wind tunnel. That is, they still appear rough with not a lot of smoothing evident after saltating over a distance of 8 m. This would suggest that they do have a lot of resistance to abrasion or material strength. However, the tiny striations evident on the surface of the particles shown in Fig. 3.2 f are suggestive of abrasion that may have arisen from their rolling or sliding along the bed surface as creep. This further demonstrates that saltation was not the only form of particle transport.

With distances of transport on Owens Lake being perhaps two orders of magnitude larger than the fetch distance in this study, a more noticeable change in aggregate surface texture might be expected. However, the three factors favouring particle spalling are balanced by mass loss associated with unsuccessful rebounds, energy loss associated with fracture

development, lower momentum or kinetic energy associated the impacts of smaller particles (Kok et al., 2012), and the fact that some particles are simply large sand grains with dust coats (i.e., SEM images in Figs. 3.1 a-h demonstrates the presence of large smooth sand grains with a dust coat). Gillette (1981) suggested smaller particles do not have enough momentum to break down and release dust, which could explain the drop off in dust production at 8 m in Figs. 3.17 a-c, where the aggregates have been reduced to about half their original diameter. When particle aggregates are transported over a very short distance, the observed constant comminution rate may arise from a balance of the positive and negative feedback described herein. Over longer distances one might expect there to be an upper limit to the amount of breakdown that occurs. To address this, Bullard et al., (2004) undertook a series of abrasion chamber experiments to determine the potential for the abrasion of dune sands to produce finer particles by their spalling or chipping, or through the release of surface grains. The purpose was to simulate abrasion resulting from saltation with the experiments substituting time for distance. They found dust production increases exponentially over time but drops off with continued abrasion. Thus, the dust production and particle diameter change over time was not fetch constrained. This experimental approach is informative, although a wind tunnel clearly provides a more accurate representation of the saltation kinetics.

The present study did not directly measure aggregate strength, stability, or resistance to abrasion since it was not feasible within the scope and timeline of the study; however, these factors could be measured as an extension of this work. On the other hand, the mineralogy and geochemistry of the aggregates can provide some insight. The salts contained within this sediment (halite and calcium carbonate) act as cement, as well as other minerals such as hydrophilite, as a result of the chemical influence on interparticle force. As discussed by Nimmo (2013) and Nield et al., (2016), saline or sodic water percolates through playa sediments and evaporates within the pore spaces, so that the evaporate minerals can lightly

cement the other grains. The T10 sediment selected for the wind tunnel experiments cannot be confirmed to be saline or sodic without measuring the SAR or ESP of the sediment, which should be done as an extension of this work. The XRD data show more calcium carbonate ($CaCl_2$) than halite (NaCl), suggesting the aggregates are cemented stronger than if halite were to be the dominating salt in this sediment. Halite is sodium based, which can weaken bonding, while chemical precipitates are susceptible to destruction from rainfall or physical disturbance (Nimmo, 2013). Overall, it is likely that the grains can easily produce or lose silt based on mineral composition. This information is important in identifying aggregate strength in order to fully support the hypotheses pertaining to and confirming aggregate breakdown.

4.2 Stokes Law and PM_{10}

The tendency for dust to settle (D) is offset in part by suspension (S) within vortices traveling with the boundary-layer flow. This determines the mass balance for a given control volume, i.e., material either accumulates when D>S, fluxes are balanced so there is no net change when D=S, and lift is very strong keeping most material aloft when D<S. Stokes law and opposing forces (i.e., turbulence) are the main drivers of particles moving up or down in a flow. Particles will naturally settle as described by Stokes Law. The projected settling velocity of the pulverized silt was estimated using Stokes Law to be 0.1 ms^{-1},

$$V_t = gd^2(\rho_p - \rho_m)/18\mu \#(E6)$$

where g is gravitational acceleration at 9.8 ms^{-2}, d particle diameter in m (0.00001 m), ρ_p particle density in $kg \cdot m^{-3}$, ρ_m density of air in $kg \cdot m^{-3}$, and μ viscosity in $kg \cdot m^{-1}s^{-1}$. This determines in part the concentration of particles 10 μm and smaller.

Notably, the projected settling velocity and the measured distribution of the vertical component of the wind velocity are of equal magnitude, clearly supporting the potential for the airflow structure to strongly affect the settling or resuspension particles in the wind tunnel. The potential for deposition to occur is clearly evident 6 m downwind, where the vertical component velocity is directed downward, whereas the suspension or resuspension of silt is most likely to occur at 8 m where there is an upward directed velocity. In examining the particle concentration data, there is good agreement with the expected trend from the flow structure profiling. The data from the experiments with pulverized silt as well as the particle speed data confirm that the concentration is affected by the upwelling versus downwelling of the airflow. The particles seem to follow a very similar trend to the flow seen in the isovel plots (Fig. 3.3). Also, since the concentration decreases to an almost undetectable level at 6 m, this can be explained in part by the deposition of silt. At 8 m the concentration increases to half of that sampled near the point of release, clearly supporting the claim that silt produced from aggregate spalling is being effectively dispersed, although the fluid stress on the bed can also affect the resuspension of dust as well.

Unlike the glass slide measurements showing aggregate breakdown, surface roughness appears to have had a significant influence on the settling and resuspension of dust. This outcome supports H4 (dust dispersion is enhanced by increasing surface roughness) since the dust concentration was higher over the rough bed surface than the smooth. This suggests that the enhancement of particle suspension with increased bed roughness is associated with greater turbulence intensity and shear stress (u_*) on the bed surface, not aggregate breakdown. To confirm the enhancement is associated with greater turbulence intensity, the LDA data, including the root mean square (RMS) and turbulence intensity, must be examined in further study. The u_* values underpinning this relationship lie between 0.31 and 0.44 ms^{-1}

for the smooth floor and between 0.39 and 0.45 ms^{-1} for the rough floor. Gelbart and Katra (2020) measured shear velocities at which particles in the silt range were more productive in producing dust. They found increasing concentrations of PM_{10} with an increasing shear velocity between 0.24 and 0.52 ms^{-1}. Therefore, the higher shear velocity attributed to the rough floor would also explain the higher concentration of PM_{10}.

4.3 Saltation and Dust Production

The main mechanism that drove the dust emission was fracturing of the aggregates during saltation. In the 500 µm experiments, the emission of dust occurred only when the saltation began; that is, when the wind speed exceeded the fluid threshold velocity for the sample. This research project used a point source drop tube for particle delivery, so that all particles were able to saltate or roll down the tunnel when the wind speed exceeded the impact threshold. The alternate purpose of the drop tube was to constrain the starting point to evaluate the net distance of travel. When the particles hit the surface at their terminal velocity, a small amount of momentum was partitioned into a ricochet. In a natural system, this momentum would come from being struck by another particle, where they would then be accelerated by the wind or remain on the surface moving as creep.

As shown in Figs. 3.11 and 3.12 the PM_{10} fluxes for the saltating aggregates are an order of magnitude lower yet still show similar trends downwind to the pulverized silt (Figs. 3.8 and 3.9). This is not in good agreement with the expected trend since it is not necessarily suggestive of a secondary dust source, i.e., breakdown. It does suggest that the dust is being affected by an artifact of the wind tunnel flow since similar trends seen in the silt experiments proved to arise from the effects of turbulence intensity and fluid stress. However, normalizing

the data removes these effects and instead focuses on the efficiency of the abrasion that occurred when saltators were blown through the wind tunnel. The normalized mass ratio in Fig. 3.14 further shows that dust production from aggregate breakdown generally increased downwind, directly supporting H3 (dust production will increase exponentially with increasing distance of transport). Measurements of the normalized index (E) indicate that when transported over a non-emissive surface, the 500 µm particles emit only 1- 4% of the dust that is suspended during the transport of an equivalent volume of disaggregated silt. Relative humidity was not found to affect dust production, potentially simplifying models of dust emission from playa systems.

Surface roughness in the saltation experiments is important to acknowledge as it not only seems to play a more important role in the mass transport rate than observed with the pulverized silt, but it also seems to have a greater effect on the mass ratio. The results shown in Figs. 3.9 and 3.12 support H4, which predicts that dust dispersion increases with an increase in surface roughness. The mass transport rate for both the pulverized silt (Fig. 3.9) and saltating particles (Fig. 3.12) show similar trends with no apparent effect of humidity. However, the results for the rough floor at a high wind speed (11 ms^{-1}) (Fig. 3.12 e) indicates that there is a significant change with distance downwind and an immediate and very large input of dust from the drop tube with an apparent effect of humidity. This suggests an enhancement of dust generation and dispersion arising from several factors. First, surface asperities affect rupture during an impact. Second, roughness generates turbulence which is critical for dust suspension. Last, roughness can also trap or shelter dust, preventing it from being suspended or resuspended. Similar studies such as Sweeney et al. (2008) measured dust emissions over surfaces varying in roughness using a PI-SWERL and a portable suction type wind tunnel. Sweeney et al. (2008) found that soils with a fine soil aggregate population had

a high potential for dust emissions. However, their results suggest texture is not a directly relevant parameter for predicting the potential for dust emission. Texture was found to play a more indirect role because crusts that limit saltation, and hence dust production, are more liable to form on fine textured soils than on coarse textured ones.

Interestingly, the mass ratio drops off after reaching a peak at 6 m downwind, but the rate of dust production continues to increase linearly with distance over the rough floor. This suggests that fetch presents a greater limitation for the smooth floor as compared to the rough one. It might be inferred from this that there was more abrasion in the experiments with the rough surface, allowing the particles to continually fracture and produce dust. However, the total fetch is limited in all experiments, and we are unable to determine what happens beyond a distance of 8 m. Over a longer distance the rate of dust production over a rough surface in strong winds could slow and drop off as well. In regard to this, Bullard et al., (2004) and others (Wright et al., 1998; Whalley et al., 1987) undertook laboratory experiments to examine the production of silt sized particles from sand as a result of aeolian abrasion. They report that for all their samples, there was a high initial rate of dust production, but it slowed down with continued abrasion. Bullard et al., (2004) interpret this phenomenon to arise from continued removal of a finite number of protuberances on the particle surfaces. In other words, the supply of silt sized grains is exhausted from the dust coat or from reduced fracturing as the particles become more rounded. This explanation is in agreement with the results obtained over the smooth floor but not that of the rough, pointing out a need for further testing that is less constrained by fetch. This could involve recycling the aggregates by collecting them at the end of the tunnel and dropping them back down the delivery tube near the working section entrance.

4.4 Summary

This study is the first of its kind to isolate the effects of aggregates on dust production and track aggregate breakdown using glass slides and microscopy. The use of the wind tunnel to examine the dust emission may not reflect the natural wind in the field where the velocity and direction are constantly changing, and fetch is not constrained. However, results from this work clearly show that particle aggregation is highly effective at reducing dust emission. These findings may be useful for air quality modelers and managers working to mitigate dust emission. The findings provide insight into soil aggregation as a key factor in determining soil erosion and dust emission potential.

Chapter Five: Conclusions

Using playa sediments obtained from Owens Lake, we isolated the effect of aggregate breakdown and dust production by saltating these over non-emissive surfaces of varied roughness. Aside from Swet and Katra (2016) and Gelbart and Katra (2020), aggregate disintegration has not been directly quantified in relation to dust production during aeolian transport. The experimental results suggest while some aggregate fracture and dust release occurs, the formation of particle aggregates within a playa surface is generally highly effective at reducing emissions. Chemistry and minerology would seem to play a large role in influencing the aggregate strength and susceptibility to fracture. The large amount of chemical precipitate contained in the test sediment (T10) is suggestive of weak cementing. Precision surface wetting at Owens Lake may be able to provide effective dust control by promoting sediment aggregation, consequently reducing water consumption as compared to shallow flooding. Future work should aim to i) measure the aggregate strength using a penetrometer, and ii) reduce the fetch limitation through either recycling the aggregates through the wind tunnel or using an abrasion chamber.

References

Alfaro, S. C., & Gomes, L. (2001). Modeling mineral aerosol production by wind erosion: Emission intensities and aerosol size distributions in source areas. Journal of Geophysical Research: Atmospheres, 106(D16), 18075-18084.

Amézketa, E. (1999). Soil aggregate stability: a review. Journal of sustainable agriculture, 14(2-3), 83-151.

Avecilla, F., Panebianco, J. E., & Buschiazzo, D. E. (2016). A wind-tunnel study on saltation and PM10 emission from agricultural soils. Aeolian research, 22, 73-83.

Bagnold, R. A. (1941). The physics of blown sand and desert dunes: New York. William Morrow & Company.

Barone, J. B., Ashbaugh, L. L., Kusko, B. H., & Cahill, T. A. (1981). The effect of Owens Dry Lake on air quality in the Owens Valley with implications for the Mono Lake area.

Bhaganagar, K., Kim, J., & Coleman, G. (2004). Effect of roughness on wall-bounded turbulence. *Flow, turbulence and combustion*, *72*(2), 463-492.

Brouwer, C., Goffeau, A., & Heibloem, M. (1985). Irrigation water management: training manual no. 1-introduction to irrigation. Food and Agriculture Organization of the United Nations, Rome, Italy, 102-103.

Bullard, J. E., McTainsh, G. H., & Pudmenzky, C. (2004). Aeolian abrasion and modes of fine particle production from natural red dune sands: an experimental study. Sedimentology, 51(5), 1103-1125.

Cahill, T. A., Gill, T. E., Gillette, D. A., Reid, E. A., Reid, J. S., & Yau, M. L. (1994). Generation, characterization and transport of Owens (dry) Lake, final report, Contract A132-105, Calif. Air Resourc. Board, Sacramento.

Cahill, T. A., Gill, T. E., Reid, J. S., Gearhart, E. A., & Gillette, D. A. (1996). Saltating particles, playa crusts and dust aerosols at Owens (dry) Lake, California. Earth Surface Processes and Landforms, 21(7), 621-639.

Chadwick, O. A., & Quick, D. J. Aeolian Additions: The Downwind Effects on Soil and Vegetation in Owens Valley.

Dahlgren, R. A., Richards, J. H., & Yu, Z. (1997). Soil and groundwater chemistry and vegetation distribution in a desert playa, Owens Lake, California. *Arid Land Research and Management*, *11*(3), 221-244.

Dantec Dynamics. (2021, March 25). Flowexplorer - Dantec Dynamics: Precision Measurement Systems & Sensors. Dantec Dynamics | Precision Measurement Systems & Sensors. Retrieved November 1, 2022, from https://www.dantecdynamics.com/solutions-applications/solutions/fluid-mechanics/laser-doppler-anemometry-lda/flowexplorer/

Duniway, M. C., Pfennigwerth, A. A., Fick, S. E., Nauman, T. W., Belnap, J., & Barger, N. N. (2019). Wind erosion and dust from US drylands: a review of causes, consequences, and solutions in a changing world. Ecosphere, 10(3), e02650.

Fécan, F., Marticorena, B., & Bergametti, G. (1998, December). Parametrization of the increase of the aeolian erosion threshold wind friction velocity due to soil moisture for arid and semi-arid areas. In Annales Geophysicae (Vol. 17, No. 1, pp. 149-157). Springer-Verlag.

Font, K. R. (1995). Geochemical and isotopic evidence for hydrologic processes at Owens Lake, California (Doctoral dissertation, University of Nevada, Reno).

Freedman, A., Gross, A., Shelef, O., Rachmilevitch, S., & Arnon, S. (2014). Salt uptake and evapotranspiration under arid conditions in horizontal subsurface flow constructed wetland planted with halophytes. *Ecological Engineering*, *70*, 282-286.

Gelbart, G., & Katra, I. (2020). Dependence of the dust emission on the aggregate sizes in loess soils. Applied Sciences, 10(16), 5410.

Gill, T. E., & Gillette, D. A. (1991). Owens Lake: A natural laboratory for aridification, playa desiccation and desert dust. In Geological Society of America Abstracts with Programs (Vol. 23, No. 5, p. 462). Boulder, CO: Geological Society of America.

Gill, T. E., & Cahill, T. A. (1992). Playa-generated dust storms from Owens Lake. HallJr. Jr., CA, Doyle-Jones, V., Widawski, B.(Eds.), The History of Water: Eastern Sierra Nevada, Owens Valley, White Inyo Mountains. University of California Press, Los Angeles, 63-73.

Gill, T. E., Gillette, D. A., Niemeyer, T., & Winn, R. T. (2002). Elemental geochemistry of wind-erodible playa sediments, Owens Lake, California. Nuclear Instruments and Methods in Physics Research Section B: Beam Interactions with Materials and Atoms, 189(1-4), 209-213.

Gillette, D. A. (1981). Production of dust that may be carried great distances. Desert dust: Origin, characteristics, and effect on man, 186, 11-26.

Gillette, D. A., Fryrear, D. W., Gill, T. E., Ley, T., Cahill, T. A., & Gearhart, E. A. (1997). Relation of vertical flux of particles smaller than 10 μm to total aeolian horizontal mass flux at Owens Lake. *Journal of Geophysical Research: Atmospheres*, *102*(D22), 26009-26015.

Gordon, M., & McKenna Neuman, C. (2009). A comparison of collisions of saltating grains with loose and consolidated silt surfaces. Journal of Geophysical Research: Earth Surface, 114(F4).

Hollett, K. J., Danskin, W. R., McCaffrey, W. F., & Walti, C. L. (1991). Geology and Water Resources of Owens Valley, California. US Geological Survey Water Supply Paper 2370–B. *B1–B77*.

Kok, J. F. (2011). A scaling theory for the size distribution of emitted dust aerosols suggests climate models underestimate the size of the global dust cycle. Proceedings of the National Academy of Sciences, 108(3), 1016-1021.

Kok, J. F., Parteli, E. J., Michaels, T. I., & Karam, D. B. (2012). The physics of wind-blown sand and dust. Reports on progress in Physics, 75(10), 106901.

Manisalidis, I., Stavropoulou, E., Stavropoulos, A., & Bezirtzoglou, E. (2020). Environmental and health impacts of air pollution: a review. Frontiers in public health, 8.

McGowan, H., & Clark, A. (2008). Identification of dust transport pathways from Lake Eyre, Australia using Hysplit. Atmospheric Environment, 42(29), 6915-6925.

McKenna Neuman, C. (2003). Effects of temperature and humidity upon the entrainment of sedimentary particles by wind. Boundary-Layer Meteorology, 108(1), 61-89.

McKenna Neuman, C., & Sanderson, S. (2008). Humidity control of particle emissions in aeolian systems. Journal of Geophysical Research: Earth Surface, 113(F2).

McKenna Neuman, C. (2016). TEWT. Retrieved November 16, 2020, from https://tuspace.ca/~cmckneuman/website/facilities.html

McKenna Neuman, C., Nickling, W., & O'Brien, P. (2018). (rep.). Wind Tunnel Study to Investigate the Efficacy of Water Content and Humidity as Controls of Particle Entrainment and Dust Emission from Owens Lake Surface Sediments, 11–67. Cambridge, ON: Nickling Environmental Limited.

Motic. (n.d.). Microscopes, Moticams and accessories. Motic Microscopes. Retrieved November 1, 2022, from https://moticmicroscopes.com/

National Academies of Sciences, Engineering, and Medicine 2020. Effectiveness and Impacts of Dust Control Measures for Owens Lake. Washington, DC: The National Academies Press. https://doi.org/10.17226/25658

Nickling, W. G., & Neuman, C. M. (1995). Development of deflation lag surfaces. Sedimentology, 42(3), 403-414.

Nield, J. M., Neuman, C. M., O'Brien, P., Bryant, R. G., & Wiggs, G. F. (2016). Evaporative sodium salt crust development and its wind tunnel derived transport dynamics under variable climatic conditions. Aeolian Research, 23, 51-62.

Nimmo, J. R. (2004). Aggregation: physical aspects. *Encyclopedia of soils in the environment. Academic Press, London, 10,* B0-12.

Ono, D., Kiddoo, P., Howard, C., Davis, G., & Richmond, K. (2011). Application of a combined measurement and modeling method to quantify windblown dust emissions from the exposed playa at Mono Lake, California. *Journal of the Air & Waste Management Association*, *61*(10), 1036-1045.

Puget, P., Chenu, C., & Balesdent, J. (2000). Dynamics of soil organic matter associated with particle-size fractions of water-stable aggregates. *European Journal of Soil Science*, *51*(4), 595-605.

Reheis, M. C. (1997). Dust deposition downwind of Owens (dry) Lake, 1991–1994: Preliminary findings. Journal of Geophysical Research: Atmospheres, 102(D22), 25999-26008.

Reid, J. S., Flocchini, R. G., Cahill, T. A., Ruth, R. S., & Salgado, D. P. (1994). Local meteorological, transport, and source aerosol characteristics of late autumn Owens Lake (dry) dust storms. Atmospheric environment, 28(9), 1699-1706.

Rieke, E. L., Bagnall, D. K., Morgan, C. L., Flynn, K. D., Howe, J. A., Greub, K. L., ... & Honeycutt, C. W. (2022). Evaluation of aggregate stability methods for soil health. *Geoderma*, *428*, 116156.

Roney, J. A., & White, B. R. (2006). Estimating fugitive dust emission rates using an environmental boundary layer wind tunnel. Atmospheric Environment, 40(40), 7668-7685.

Schlaepfer, D. R., Bradford, J. B., Lauenroth, W. K., Munson, S. M., Tietjen, B., Hall, S. A., ... & Jamiyansharav, K. (2017). Climate change reduces extent of temperate drylands and intensifies drought in deep soils. Nature Communications, 8(1), 1-9.

Selva, T. M. G., Selva, J. S. G., & Prata, R. B. (2021). Sensing Materials: Diamond-Based Materials.

Shao, Y., Raupach, M. R., & Findlater, P. A. (1993). Effect of saltation bombardment on the entrainment of dust by wind. Journal of Geophysical Research: Atmospheres, 98(D7), 12719-12726.

Shao, Y. (2001). A model for mineral dust emission. Journal of Geophysical Research: Atmospheres, 106(D17), 20239-20254.

Shao, Y. (2004). Simplification of a dust emission scheme and comparison with data. Journal of Geophysical Research: Atmospheres, 109(D10).

Shao, Y. (2008). Physics and Modelling of Wind Erosion. In Atmospheric and Oceanographic Sciences Library (2nd ed.). Springer.

Sweeney, M., Etyemezian, V., Macpherson, T., Nickling, W., Gillies, J., Nikolich, G., & McDonald, E. (2008). Comparison of PI-SWERL with dust emission measurements from a straight-line field wind tunnel. Journal of Geophysical Research: Earth Surface, 113(F1).

Swet, N., & Katra, I. (2016). Reduction in soil aggregation in response to dust emission processes. Geomorphology, 268, 177-183.

Tatarko, J. (2001). Soil aggregation and wind erosion: processes and measurements. Annals of arid zone, 40(3), 251-264.

US Department of Commerce. (2022, March 3). *Climate*. NOAA's National Weather Service. Retrieved January 13, 2023, from https://www.weather.gov/wrh/climate

Wang, H. T., Zhou, Y. H., Dong, Z. B., & Ayrault, M. (2008). Vertical dispersion of dust particles in a turbulent boundary layer. Earth Surface Processes and Landforms: The Journal of the British Geomorphological Research Group, 33(8), 1210-1221.

Whalley, W. B., Smith, B. J., McAlister, J. J., & Edwards, A. J. (1987). Aeolian abrasion of quartz particles and the production of silt-size fragments: preliminary results. Geological Society, London, Special Publications, 35(1), 129-138.

Wright, J., Smith, B., & Whalley, B. (1998). Mechanisms of loess-sized quartz silt production and their relative effectiveness: laboratory simulations. Geomorphology, 23(1), 15-34.

Xiao, J., & Taylor, P. A. (2002). On equilibrium profiles of suspended particles. Boundary-Layer Meteorology, 105(3), 471-482.

Zhong, S., Li, J., Whiteman, C. D., Bian, X., & Yao, W. (2008). Climatology of high wind events in the Owens Valley, California. Monthly weather review, 136(9), 3536-3552.

Appendix I

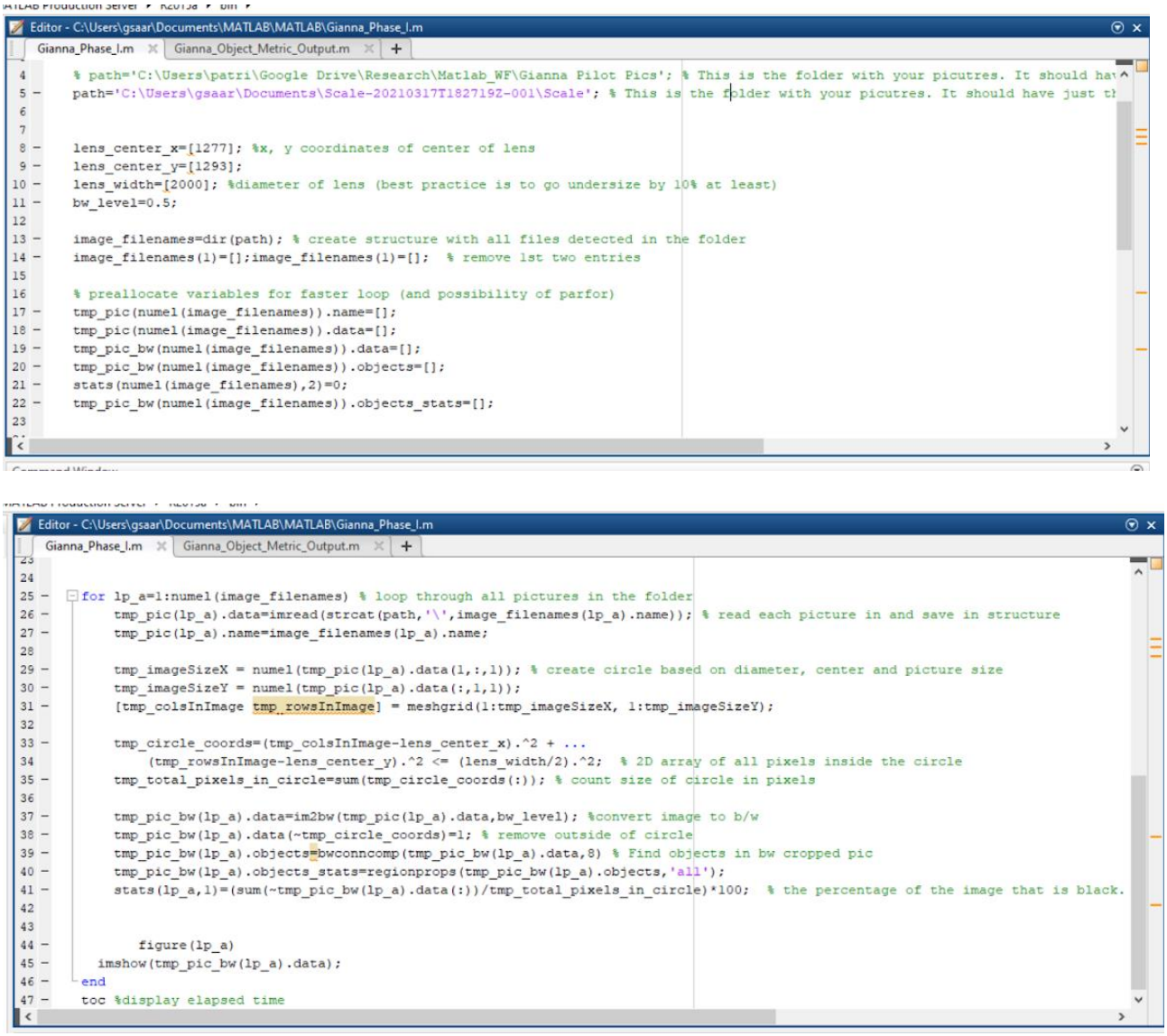

```
Editor - C:\Users\gsaar\Documents\MATLAB\MATLAB\Gianna_Phase_I.m
Gianna_Phase_I.m | Gianna_Object_Metric_Output.m

% path='C:\Users\patri\Google Drive\Research\Matlab_WF\Gianna Pilot Pics'; % This is the folder with your picutres. It should hav
path='C:\Users\gsaar\Documents\Scale-20210317T182719Z-001\Scale'; % This is the folder with your picutres. It should have just th


lens_center_x=[1277]; %x, y coordinates of center of lens
lens_center_y=[1293];
lens_width=[2000]; %diameter of lens (best practice is to go undersize by 10% at least)
bw_level=0.5;

image_filenames=dir(path); % create structure with all files detected in the folder
image_filenames(1)=[];image_filenames(1)=[];  % remove 1st two entries

% preallocate variables for faster loop (and possibility of parfor)
tmp_pic(numel(image_filenames)).name=[];
tmp_pic(numel(image_filenames)).data=[];
tmp_pic_bw(numel(image_filenames)).data=[];
tmp_pic_bw(numel(image_filenames)).objects=[];
stats(numel(image_filenames),2)=0;
tmp_pic_bw(numel(image_filenames)).objects_stats=[];
```



```
Editor - C:\Users\gsaar\Documents\MATLAB\MATLAB\Gianna_Phase_I.m
Gianna_Phase_I.m | Gianna_Object_Metric_Output.m


for lp_a=1:numel(image_filenames) % loop through all pictures in the folder
    tmp_pic(lp_a).data=imread(strcat(path,'\',image_filenames(lp_a).name)); % read each picture in and save in structure
    tmp_pic(lp_a).name=image_filenames(lp_a).name;

    tmp_imageSizeX = numel(tmp_pic(lp_a).data(1,:,1)); % create circle based on diameter, center and picture size
    tmp_imageSizeY = numel(tmp_pic(lp_a).data(:,1,1));
    [tmp_colsInImage tmp_rowsInImage] = meshgrid(1:tmp_imageSizeX, 1:tmp_imageSizeY);

    tmp_circle_coords=(tmp_colsInImage-lens_center_x).^2 + ...
        (tmp_rowsInImage-lens_center_y).^2 <= (lens_width/2).^2;  % 2D array of all pixels inside the circle
    tmp_total_pixels_in_circle=sum(tmp_circle_coords(:)); % count size of circle in pixels

    tmp_pic_bw(lp_a).data=im2bw(tmp_pic(lp_a).data,bw_level); %convert image to b/w
    tmp_pic_bw(lp_a).data(~tmp_circle_coords)=1; % remove outside of circle
    tmp_pic_bw(lp_a).objects=bwconncomp(tmp_pic_bw(lp_a).data,8) % Find objects in bw cropped pic
    tmp_pic_bw(lp_a).objects_stats=regionprops(tmp_pic_bw(lp_a).objects,'all');
    stats(lp_a,1)=(sum(~tmp_pic_bw(lp_a).data(:))/tmp_total_pixels_in_circle)*100;  % the percentage of the image that is black.


      figure(lp_a)
  imshow(tmp_pic_bw(lp_a).data);
end
 toc %display elapsed time
```

Appendix 1.1. The figures above depict the MATLAB code used to output the images in Appendix 1.3 and 1.5 called ‘Gianna_Phase_I’.

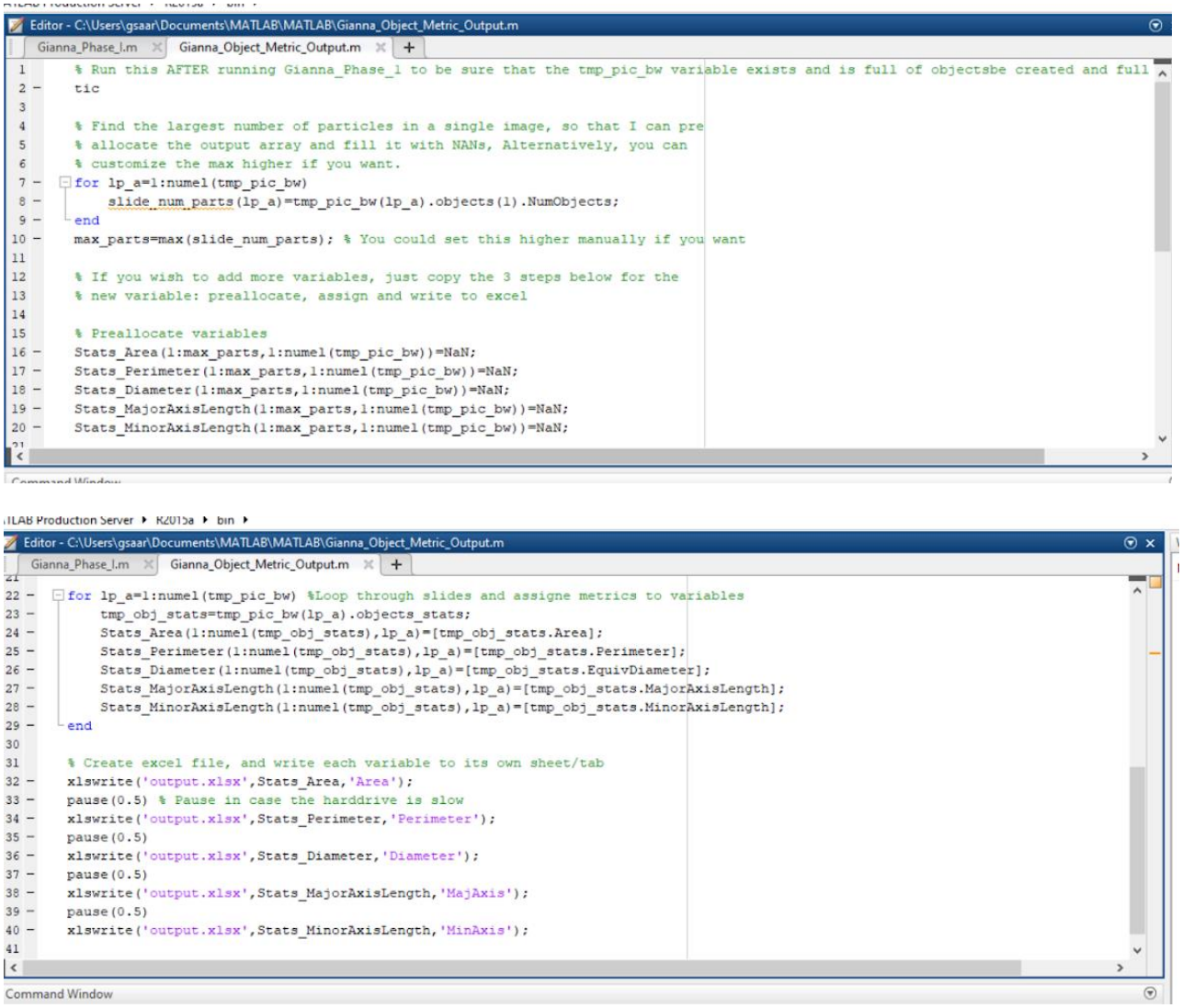

```
Editor - C:\Users\gsaar\Documents\MATLAB\MATLAB\Gianna_Object_Metric_Output.m
Gianna_Phase_l.m | Gianna_Object_Metric_Output.m

1   % Run this AFTER running Gianna_Phase_1 to be sure that the tmp_pic_bw variable exists and is full of objectsbe created and full
2   tic
3
4   % Find the largest number of particles in a single image, so that I can pre
5   % allocate the output array and fill it with NANs, Alternatively, you can
6   % customize the max higher if you want.
7   for lp_a=1:numel(tmp_pic_bw)
8       slide_num_parts(lp_a)=tmp_pic_bw(lp_a).objects(1).NumObjects;
9   end
10  max_parts=max(slide_num_parts); % You could set this higher manually if you want
11
12  % If you wish to add more variables, just copy the 3 steps below for the
13  % new variable: preallocate, assign and write to excel
14
15  % Preallocate variables
16  Stats_Area(1:max_parts,1:numel(tmp_pic_bw))=NaN;
17  Stats_Perimeter(1:max_parts,1:numel(tmp_pic_bw))=NaN;
18  Stats_Diameter(1:max_parts,1:numel(tmp_pic_bw))=NaN;
19  Stats_MajorAxisLength(1:max_parts,1:numel(tmp_pic_bw))=NaN;
20  Stats_MinorAxisLength(1:max_parts,1:numel(tmp_pic_bw))=NaN;
```



```
TLAB Production Server ▸ R2015a ▸ bin ▸
Editor - C:\Users\gsaar\Documents\MATLAB\MATLAB\Gianna_Object_Metric_Output.m
Gianna_Phase_l.m | Gianna_Object_Metric_Output.m

22  for lp_a=1:numel(tmp_pic_bw) %Loop through slides and assigne metrics to variables
23      tmp_obj_stats=tmp_pic_bw(lp_a).objects_stats;
24      Stats_Area(1:numel(tmp_obj_stats),lp_a)=[tmp_obj_stats.Area];
25      Stats_Perimeter(1:numel(tmp_obj_stats),lp_a)=[tmp_obj_stats.Perimeter];
26      Stats_Diameter(1:numel(tmp_obj_stats),lp_a)=[tmp_obj_stats.EquivDiameter];
27      Stats_MajorAxisLength(1:numel(tmp_obj_stats),lp_a)=[tmp_obj_stats.MajorAxisLength];
28      Stats_MinorAxisLength(1:numel(tmp_obj_stats),lp_a)=[tmp_obj_stats.MinorAxisLength];
29  end
30
31  % Create excel file, and write each variable to its own sheet/tab
32  xlswrite('output.xlsx',Stats_Area,'Area');
33  pause(0.5) % Pause in case the harddrive is slow
34  xlswrite('output.xlsx',Stats_Perimeter,'Perimeter');
35  pause(0.5)
36  xlswrite('output.xlsx',Stats_Diameter,'Diameter');
37  pause(0.5)
38  xlswrite('output.xlsx',Stats_MajorAxisLength,'MajAxis');
39  pause(0.5)
40  xlswrite('output.xlsx',Stats_MinorAxisLength,'MinAxis');
41

Command Window
```

Appendix 1.2. The figures above depict the MATLAB code used to output an excel file that provided the data for creating the data shown in Fig 3.8 called ‘Gianna_Object_Metric_Output’.

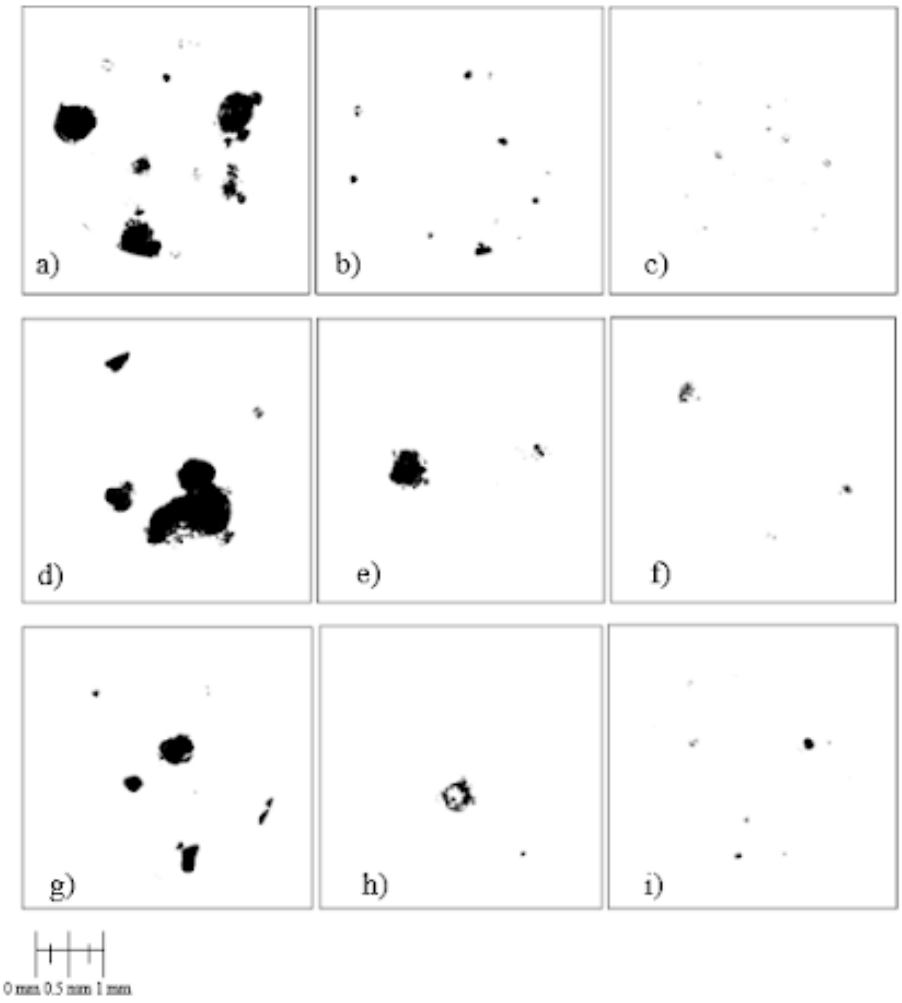

Appendix 1.3 a-i. Sample MATLAB output figures of 3 replicates for glycerol slides 1 (furthest upwind slide), slides 6 (middle), and 12 (furthest downwind slide) using 500 µm aggregates.

BW%	Slide 1	Slide 6	Slide 12
Replicate 1	11.33 (A 1.3a)	0.91 (A 1.3b)	0.15 (A 1.3c)
Replicate 2	13.21 (A 1.3d)	2.66 (A 1.3e)	0.42 (A 1.3f)
Replicate 3	3.91 (A 1.3g)	1.06 (A 1.3h)	0.38 (A 1.3i)

Appendix 1.4. Summary table of the percentage of black to white pixels for Appendix 1.3 a-i.

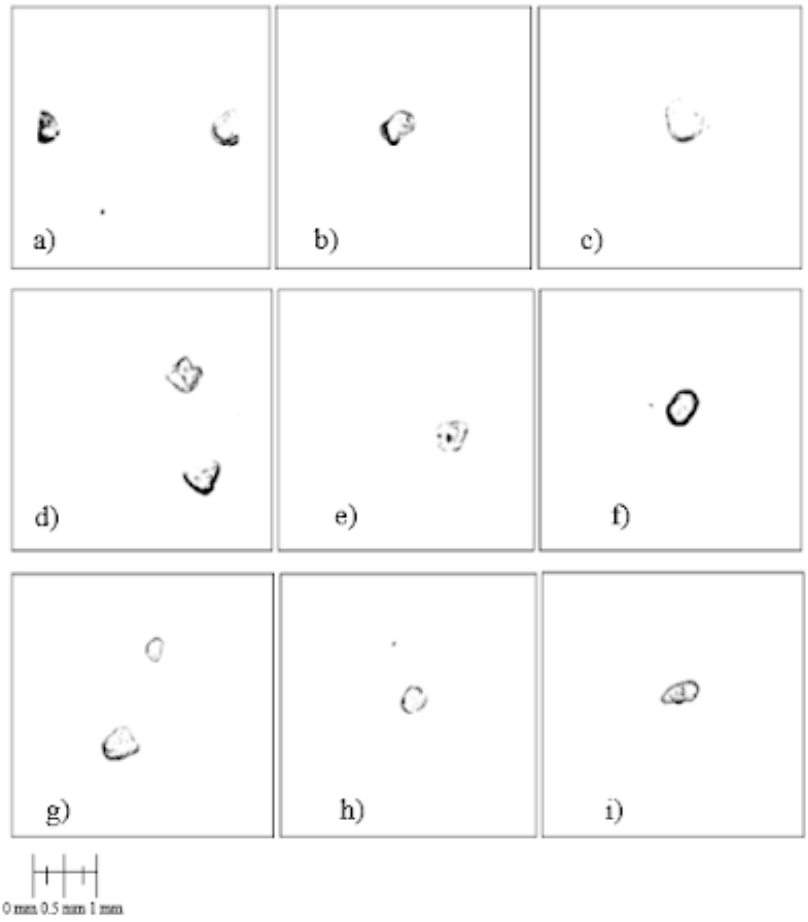

Appendix 1.5 a-i. MATLAB Output Figures of 3 replicates for glycerol slides 1 (furthest upwind slide), slides 6 (middle), and 12 (furthest downwind slide) using 500 µm control sand.

BW%	Slide 1	Slide 6	Slide 12
Replicate 1	0.79 (A 1.5a)	0.41 (A 1.5b)	0.51 (A 1.5c)
Replicate 2	1.38 (A 1.5d)	1.00 (A 1.5e)	1.59 (A 1.5f)
Replicate 3	0.89 (A 1.5g)	0.40 (A 1.5h)	0.76 (A 1.5i)

Appendix 1.6. Summary table of the percentage of black to white pixels for Appendix 1.5 a-i.

R^2	$8ms^{-1}$ 20% RH	$8ms^{-1}$ 35% RH	$8ms^{-1}$ 50% RH	$10ms^{-1}$ 20% RH	$10ms^{-1}$ 35% RH	$10ms^{-1}$ 50% RH	$11ms^{-1}$ 20% RH	$11ms^{-1}$ 35% RH	$11ms^{-1}$ 50% RH
Rough Floorboards	n/a	n/a	n/a	0.43	0.16	0.31	0.37	0.32	0.55
Smooth Floorboards	0.20	0.43	0.67	0.55	0.24	0.32	0.62	0.57	0.39

Appendix 1.7. Summary of R^2 values under varying wind speeds, humidity's, and roughness from glycerol slide analysis with 500 µm aggregates.

Slope	$8ms^{-1}$ 20% RH	$8ms^{-1}$ 35% RH	$8ms^{-1}$ 50% RH	$10ms^{-1}$ 20% RH	$10ms^{-1}$ 35% RH	$10ms^{-1}$ 50% RH	$11ms^{-1}$ 20% RH	$11ms^{-1}$ 35% RH	$11ms^{-1}$ 50% RH
Rough Floorboards	n/a	n/a	n/a	-0.039	-0.039	-0.045	-0.048	-0.056	-0.070
Smooth Floorboards	-0.016	-0.036	-0.020	-0.023	-0.041	-0.021	-0.050	-0.061	-0.056

Appendix 1.8. Summary of slope values under varying wind speeds, humidity's, and roughness from glycerol slide analysis with 500 µm aggregates.

Sand	R^2	Slope
	0.00004	-0.0001

Appendix 1.9. Summary of R^2 and slope values with 500 µm control sand.

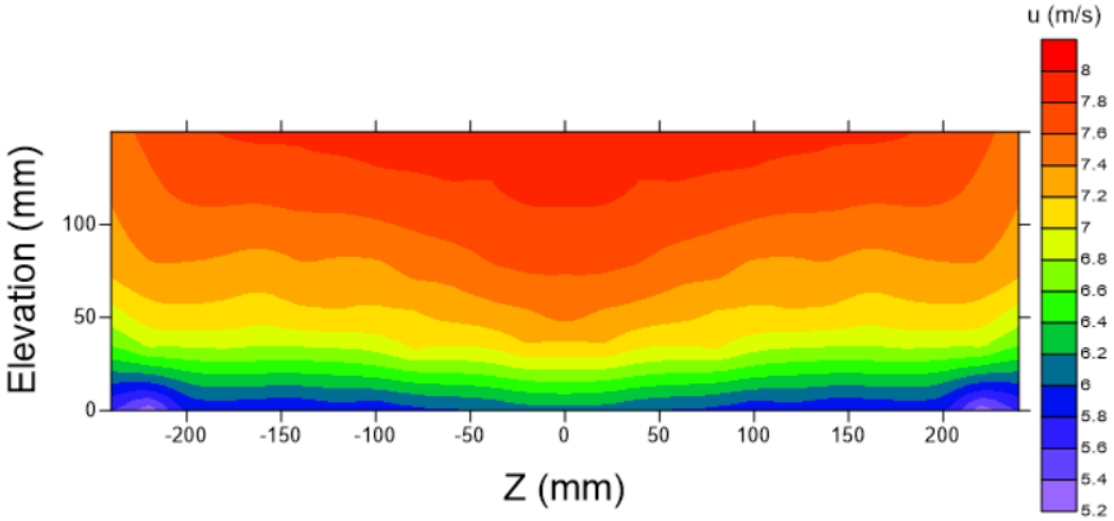

a)

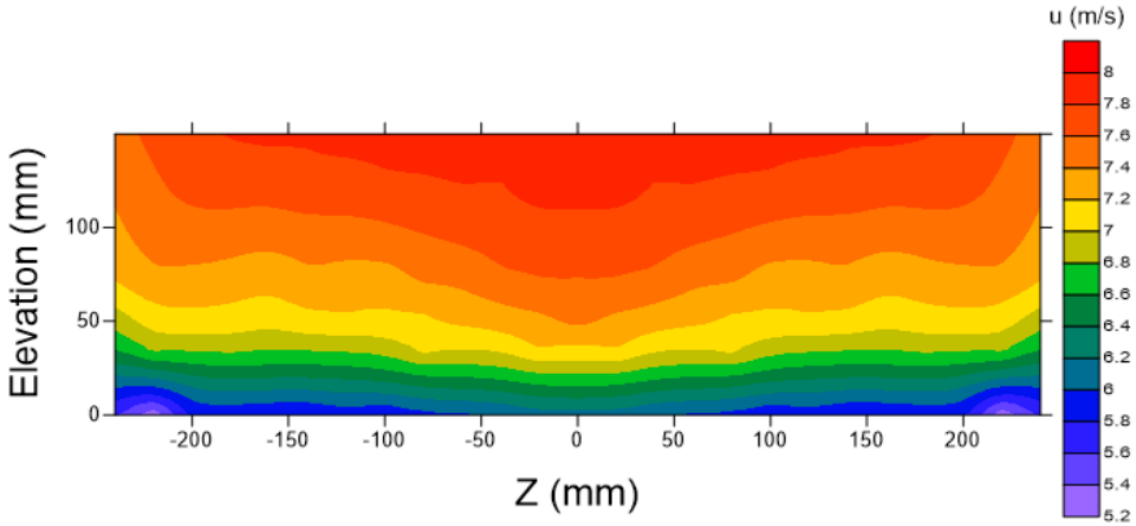

b)

Appendix 1.10 a-b. Isovel plot of the streamwise velocity along a grid plane oriented normal to the mean flow at a) 6 m and b) 8 m downwind of the sediment delivery tube.